Monthly Notices of the ROYAL ASTRONOMICAL SOCIETY

MNRAS **543,** 3345–3366 (2025) https://doi.org/10.1093/mnras/staf1516
Advance Access publication 2025 September 11

Turbulence-dominated CGM: the origin of UV absorbers with equivalent widths of ∼1 Å

Aharon Kakoly [1]★ Jonathan Stern [1] Claude-André Faucher-Giguère [2] Drummond B. Fielding [3] Roy Goldner,[1] Guochao Sun [2] and Cameron B. Hummels[4]

[1]*School of Physics and Astronomy, Tel Aviv University, Tel Aviv 69978, Israel*
[2]*Department of Physics, Astronomy and CIERA, Northwestern University, 1800 Sherman Avenue, Evanston, IL 60201, USA*
[3]*Department of Astronomy, Cornell University, Ithaca, NY 14853, USA*
[4]*TAPIR, California Institute of Technology, Mailcode 350-17, Pasadena, CA 91125, USA*

Accepted 2025 September 3. Received 2025 August 24; in original form 2025 April 24

ABSTRACT

Theoretical arguments and observations suggest that in massive haloes ($> 10^{12}\,M_\odot$), the circumgalactic medium (CGM) is dominated by a 'hot' phase with gas temperature near the virial temperature ($T \approx T_{\rm vir}$) and a quasi-hydrostatic pressure profile. Lower-mass haloes are however unlikely to be filled with a similar quasi-static hot phase, due to rapid radiative cooling. Using the FIRE (Feedback In Realistic Environment) cosmological zoom simulations, we demonstrate that the hot phase is indeed subdominant at inner radii ($\lesssim 0.3 R_{\rm vir}$) of $\lesssim 10^{12}\,M_\odot$ haloes, and the inner CGM is instead filled with $T \ll T_{\rm vir}$ gas originating in outflows and inflows, with a turbulent velocity comparable to the halo virial velocity. The turbulent velocity thus exceeds the mass-weighted sound speed in the inner CGM, and the turbulence is supersonic. UV absorption features from such CGM trace the wide lognormal density distributions of the predominantly cool and turbulent volume-filling phase, in contrast with tracing localized cool 'clouds' embedded in a hot medium. We predict equivalent widths of $W_\lambda \sim 2\lambda v_{\rm c}/c \sim 1$Å for a broad range of strong UV and EUV transitions (Mg II, C II, C IV, Si II–IV, O III–V) in sightlines through inner CGM dominated by turbulent pressure of $\lesssim L^\star$ galaxies at redshifts $0 \leq z \lesssim 2$, where λ is the transition wavelength, $v_{\rm c}$ is the circular velocity, and c is the speed of light. Comparison of our predictions with observational constraints suggests that star forming $\lesssim L^\star$ and dwarf galaxies are generally dominated by turbulent pressure in their inner CGM, rather than by thermal pressure. The inner CGM surrounding these galaxies is thus qualitatively distinct from that around quenched galaxies and massive discs such as the Milky-Way and M31, in which thermal pressure likely dominates.

Key words: turbulence – galaxies: evolution – galaxies: haloes – galaxies: ISM – quasars: absorption lines – ultraviolet: ISM.

1 INTRODUCTION

At which halo mass and redshift does a quasi-static 'hot' phase, with temperature comparable to the halo virial temperature $T_{\rm vir}$, form in the circumgalactic medium (CGM)? The development of the hot CGM phase and its implications for galaxy evolution have been the subject of classic galaxy evolution papers since the late 1970s (Rees & Ostriker 1977; Silk 1977; White & Rees 1978; White & Frenk 1991; Birnboim & Dekel 2003; Kereš et al. 2005; Dekel & Birnboim 2006). These studies argued that a hot CGM that contracts slowly on to the galaxy can form only if its cooling time exceeds the halo free-fall time, corresponding to the mass of the dark matter halo exceeding a threshold in the range $\sim 10^{11}$–$10^{12}\,M_\odot$. Since the formation of the hot CGM alters the physics of galaxy accretion and feedback, its effects on galaxy evolution are plausibly profound. Indeed, the interplay between hot CGM formation and black hole (BH) feedback has been a leading explanation for quenching of star formation, due to the increased susceptibility of the hot phase to energy deposition by BH feedback (Bower et al. 2006; Croton et al. 2006; Dekel & Birnboim 2006; Somerville et al. 2008), or due to the confinement of stellar-driven outflows by the hot CGM, which allows the central BH to grow thus enabling BH feedback (Bower et al. 2017; Byrne et al. 2023). More recent studies have argued that hot CGM formation may also facilitate the formation of thin galactic discs observed mainly at redshift $z \lesssim 1$ (Sales et al. 2012; Yu et al. 2021; Stern et al. 2021a; Hafen et al. 2022; Byrne et al. 2023; Gurvich et al. 2023; Yu et al. 2023), due to the ability of hot accreting gas to develop an aligned angular momentum distribution prior to joining the galaxy (see especially Hafen et al. 2022). These scenarios demonstrate that the hot CGM likely has a significant role in galaxy evolution, and it would thus be useful to identify its formation in observations.

Recent theoretical advances on the nature of hot CGM formation provide insight into its observational signatures. First, CGM simulations that account for stellar feedback have demonstrated that hot $T \sim T_{\rm vir}$ gas also exists at halo masses below the threshold, but is limited to transient and localized radiative shocks, in contrast with a long-lived and volume-filling hot medium at high masses (van de Voort et al. 2016; Fielding et al. 2017; Lochhaas et al. 2020; Stern

★ E-mail: aharonkakoly@mail.tau.ac.il

et al. 2020; Stern et al. 2021a; Gurvich et al. 2023; Pandya et al. 2023). This is in contrast with earlier studies which did not include feedback and associated hot CGM formation with whether a virial shock occurs at all (e.g. Birnboim & Dekel 2003). In the presence of feedback, 'hot CGM formation' is thus more accurately defined as a transition from a kinetic energy-dominated CGM (i.e. turbulence and coherent inflow/outflow) to a thermal energy-dominated CGM (Fielding et al. 2017). Secondly, recent studies have shown that the mass threshold for hot CGM formation depends on CGM radius, with a larger mass threshold of $\sim 10^{12}$ $M_\odot$ at inner CGM radii where cooling times are relatively short and a lower threshold of $\sim 10^{11}$ $M_\odot$ at outer CGM radii where cooling times are long (Stern et al. 2020; Stern et al. 2021a, b; Gurvich et al. 2023). Thus, in a given halo the quasi-static hot CGM forms first at large CGM radii and later at inner radii. This 'outside–in' hot CGM formation process is in contrast with the 'inside–out' picture suggested by the simulations of Birnboim & Dekel (2003) which did not include feedback. The transition in the inner CGM which has a higher-mass threshold, dubbed 'inner CGM virialization (ICV)', appears especially important for the evolution of the central galaxy since it changes the immediate environment in which the galaxy evolves (Stern et al. 2021a).

How can we identify if a quasi-static and long-lived hot phase exists in the inner CGM of star-forming (SF) galaxies? Addressing this question via hot phase observations can be challenging, since one needs to determine whether this phase constitutes a quasi-static volume-filling medium as expected after ICV, or rather the transient bursts originating in feedback expected prior to ICV. In the Milky-Way, observations of O VII and O VIII absorption lines in the CGM appear to require that a quasi-static hot phase indeed extends down to the galaxy (Pezzulli, Fraternali & Binney 2017; Bregman et al. 2018; Sormani et al. 2018; Stern et al. 2019; Faerman, Sternberg & McKee 2020; Singh et al. 2024; Stern et al. 2024; Sultan et al. 2024), i.e. the Milky-Way is post-ICV. A similar conclusion can be drawn for nearby massive spirals, based both on resolved X-ray emission (e.g. Anderson, Churazov & Bregman 2016) and on measurements of the thermal Sunyaev–Zeldovich (tSZ) effect (Bregman et al. 2022; Oren et al. 2024). For more distant or lower-mass galaxies where these X-ray and tSZ observations are less constraining, and especially around the low-mass and high-redshift galaxies expected to be pre-ICV, the nature of the hot phase in the inner CGM is still unclear.

An alternative method to identifying a quasi-static hot CGM directly is to infer its existence/absence from the properties of the cool CGM ($\sim 10^4$ K), a gas phase considerably more accessible to observations. Indeed, the first observational indications for a hot CGM were the inferred high thermal pressures of cool Ca II-absorbing gas around the Milky Way (Spitzer 1956). This classic result raises the question: *what are the properties of the cool CGM when the hot phase is subdominant*? Theuns (2021) and Stern et al. (2021b) addressed this question for high-redshift CGM ($z \gtrsim 3$), focusing on implications for observations of Damped Ly α absorbers (DLAs). In the present study, we focus on UV absorption signatures of pre-ICV CGM at lower redshifts of $z \lesssim 2$, at which large samples of circumgalactic absorbers and their associated galaxies are available (see below). Based on the properties of pre-ICV CGM mentioned above, we expect UV absorption features in such systems to indicate the presence of large cool gas columns and high-velocity dispersions. In the present study we quantify these predictions using the FIRE-2 (Feedback In Realistic Environment 2) cosmological zoom simulations (Hopkins et al. 2018).

The inner CGM of $\lesssim L^*$ galaxies, which is predicted to be pre-ICV, has a relatively small cross-section for sightlines to background sources in which UV absorption can be detected. Large samples of UV absorber–galaxy pairs are thus required for robust statistics, and more so given the large halo-to-halo and sightline-to-sightline variability. On the other hand, the large cool gas columns and velocity dispersions expected in pre-ICV haloes imply large absorption equivalent widths, which are detectable even in relatively low-resolution ($\sim 100\,\mathrm{km\,s^{-1}}$) spectra. Such large samples of UV absorber–galaxy pairs are available from the Sloan Digital Sky Survey (SDSS; Lan, Ménard & Zhu 2014; Lan 2020; Anand, Nelson & Kauffmann 2021) and more recently in larger numbers from the Dark Energy Survey Instrument (DESI; Wu et al. 2025), mainly in the Mg II $\lambda\lambda$2796, 2803 transition. These samples provide the main observational constraint to which we compare our predictions.

This paper is structured as follows. In Section 2, we describe the FIRE simulations and our analysis technique. Section 3 presents the predicted UV absorption properties before and after a volume-filling hot phase forms in the inner CGM. These predictions are compared to observational constraints in Section 4. We discuss our results in Section 5 and provide a summary of our main conclusions in Section 6. Throughout the paper, we use cosmological parameters from the Planck 2018 results (Aghanim et al. 2018) with Hubble parameter $H_0 = 70\,\mathrm{km\,s^{-1}\,Mpc^{-1}}$, $\Omega_\mathrm{m} = 0.3$, and $\Omega_\mathrm{b} = 0.05$.

2 METHODS

We analyse FIRE-2 simulations (Hopkins et al. 2018) in order to deduce the properties and observational signatures of circumgalactic UV absorbers prior to the formation of a quasi-static hot phase. In these simulations a hot phase forms in the inner CGM ($\sim 0.1\,R_\mathrm{vir}$, where R_vir is the halo virial radius) when the halo mass reaches $\approx 10^{12}$ $M_\odot$ (Stern et al. 2021a). We utilize the TRIDENT-v1.3 code (Hummels, Smith & Silvia 2017) to generate synthetic UV absorption spectra.

2.1 FIRE simulations

The FIRE project[1] (Hopkins et al. 2014, 2018, 2023) investigates how feedback mechanisms influence galaxy formation in cosmological simulations. We utilize the second iteration of the FIRE cosmological 'zoom' simulations (FIRE-2), which allow investigating physical processes within the CGM including the distribution and dynamics of cold and hot gas. FIRE-2 use the GIZMO code for gravity and hydrodynamics computations (Hopkins 2015) in its meshless finite-mass mode (MFM). Gravity calculations are conducted using a modified version of the Tree-PM solver, similar to the one used in GADGET-3 (Springel 2005), with adaptive softening for gas resolution elements. Gas heating and cooling processes include metal-line cooling, free–free emission, photoionization, recombination, Compton scattering with the cosmic microwave background, collisional and photoelectric heating by dust grains, and cooling processes at low temperatures ($< 10^4$ K), including molecular and fine-structure cooling. The relevant ionization states are derived from precomputed CLOUDY tables (Ferland, Korista & Verner 1998), accounting for the effects of the cosmic UV background from Faucher-Giguère et al. (2009) and galactic radiation sources (see Hopkins et al. 2018). FIRE-2 also includes a subgrid turbulent diffusion model that captures unresolved mixing of metals and thermal energy between gas resolution elements, which is important for modeling the distribution and observability of metal absorbers (Hopkins 2017; Escala et al. 2018). Star formation and stellar feedback are treated in a subgrid manner.

[1] See the FIRE project website: http://fire.northwestern.edu.

Table 1. FIRE-2 cosmological zoom simulations used in this work. (1) galaxy name; (2) mass of baryonic resolution element; (3) final redshift of the simulation; (4) central halo mass at the final redshift; (5) stellar mass of central galaxy at the final redshift; (6) redshift of ICV at which inner CGM turbulence becomes subsonic; (7) reference papers for simulations: A: El-Badry, Quataert & Wetzel (2018), B: Garrison-Kimmel et al. (2017), C: Garrison-Kimmel et al. (2019), D: Wetzel, Hopkins & Kim (2016), E: Anglés-Alcázar, Faucher-Giguère & Quataert (2017), F: Bhattarai et al. (2022), G: Samuel et al. (2020).

Name	m_b ($M_\odot$)	z_{min}	$M_{halo}(z_{min})$ ($10^{12}\,M_\odot$)	$M_*(z_{min})$ ($10^{10}\,M_\odot$)	z_{ICV}	Ref.
(1)	(2)	(3)	(4)	(5)	(6)	(7)
m12i	7100	0	1.1	7.3	0.31	D
m12b	7100	0	1.3	10	0.64	C
m12w	7100	0	0.95	6.5	0.27	G
m12c	7100	0	1.3	6.8	0.6	C
m12f	7100	0	1.5	9.7	0.63	B
m11d	7100	0	0.3	0.51	–	A
m13A1	33 000	1	4	28	3.1	E
m12i	880	0	0.9	5.7	0.62	F
m12i	57 000	0	1.2	9.1	0.98	D

Star formation occurs within self-gravitating, self-shielded molecular gas with $n_H > 1000\,cm^{-3}$ (Hopkins, Narayanan & Murray 2013). Feedback from stars is implemented through radiation pressure, heating via photoionization and photoelectric processes, and the deposition of energy, momentum, mass, and metals from supernovae and stellar winds. Feedback parameters and their time dependence are based on the stellar evolution models of Leitherer, Schaerer & Goldader (1999), assuming a Kroupa (2001) initial mass function. The simulations analysed in this work do not include feedback from active galactic nuclei (AGNs), a caveat we address in the discussion. A full description of the FIRE-2 simulations is provided in Hopkins et al. (2018).

2.2 Simulation selection

We analyse nine representative FIRE-2 simulations, as listed in Table 1. Five simulations (m12i, m12b, m12w, m12c, and m12f) have masses similar to the Milky Way, with $M_{halo} \sim 10^{12}\,M_\odot$ and an $\sim L^*$ galaxy at $z = 0$. We focus on this mass range in this paper. To explore the dependence on halo mass history, we analyse also a simulation of a dwarf galaxy halo with $M_{halo} \sim 10^{11}\,M_\odot$ at $z = 0$ (m11d) and a massive halo with $M_{halo} \sim 0.4 \cdot 10^{13}\,M_\odot$ at $z = 1$ (m13A1). This allows us to demonstrate that the formation of a quasi-static hot phase occurs earlier in more massive haloes. The typical baryonic resolution element is $m_b = 7100$–$33\,000\,M_\odot$absorption is small. For example, ensuring that subgrid prescriptions are applied at the level of giant molecular clouds or better, while $\sim L^*$ galaxy discs are resolved with $\sim 10^6$ particles. We analyse also m12i simulations with different resolutions in order to test the dependence of our main results on resolution. The virial radius R_{vir} and virial mass (M_{vir}) of the central halo in each snapshot are determined using the Amiga Halo Finder (AHF; Knollmann & Knebe 2009), based on the Bryan & Norman (1998) criterion.

2.3 Ion fractions

Ion fractions f_{ion} in the CGM were calculated as a function of gas density, temperature, metallicity, and redshift in the simulation, using the TRIDENT ionization tables which assume collisional ionization equilibrium and photoionization equilibrium from the meta-galactic ultraviolet background in Haardt & Madau (2012). Ion volume densities were then calculated using the formula:

$$n_{ion} = n_H \cdot \frac{N_X}{N_H} \cdot f_{ion}, \quad (1)$$

where n_H is the hydrogen number density and N_X/N_H represents the abundance of element X relative to hydrogen as tracked in FIRE. We focus on ions with UV transitions commonly observed in the CGM. The transitions are listed in Table 2, which includes the ion name, transition wavelength (λ), oscillator strength (f_{lu}), and N_X/N_H assuming $Z = 0.3\,Z_\odot$.

Our calculation of f_{ion} does not include the contribution of ionizing photons from young stars in the galaxy. The effect of these local sources on the ionization state of the CGM in FIRE was explored by Holguin et al. (2024) using a Monte Carlo radiation transfer code. At the radius of $0.2\,R_{vir}$ which we focus on below, they deduced a small contribution of local sources at $z < 1$ and a contribution comparable to the UV background at $1 < z < 2$. Such a factor of $\lesssim 2$ uncertainty in the ionizing background does not affect are conclusions, as discussed below.

Table 2. Absorption features discussed in this work. (1) Ion; (2) wavelength; (3) oscillator strength; (4) element abundance relative to hydrogen assuming a CGM metallicity of $0.3\,Z_\odot$; (5) ionization potential.

Ion	λ(Å)	f_{lu}	N_X/N_H ($Z = 0.3\,Z_\odot$)	χ(eV)
(1)	(2)	(3)	(4)	(5)
Si II	1260	1.22	9.7×10^{-6}	8.2
Si III	1206	1.67	″	16.3
Si IV	1403	0.255	″	33.5
Mg II	2796	0.608	1.2×10^{-5}	7.6
Mg II	2803	0.303	″	″
S III	1190	0.61	4.0×10^{-6}	23.3
O III	833	0.106	1.5×10^{-4}	35.1
O IV	788	0.111	″	54.9
O V	630	0.512	″	77.4
O VI	1031	0.133	″	113.9
C II	1335	0.127	8.1×10^{-5}	11.3
C IV	1548	0.19	″	47.9

2.4 Characteristic velocities

We demonstrate below that the formation of a quasi-static hot CGM phase implies a transition in the nature of CGM turbulence, from supersonic to subsonic. To this end we calculate several radius and time-dependent characteristic velocities in the simulation.

The circular velocity v_c at a given time and radius is calculated using

$$v_c(r,t) = \sqrt{\frac{GM(<r)}{r}}, \quad (2)$$

where G is the gravitational constant, and $M(<r)$ is the total enclosed mass within a radius r in the snapshot corresponding to time t including contributions from gas, dark matter, and stars. The mass-weighted sound speed $\langle c_s \rangle_\rho$ at a given time t and radius r is calculated via

$$\langle c_s \rangle_\rho = \cdot \frac{\sum_i m_i \sqrt{k_B T_i/(\mu m_p)}}{\sum_i m_i}, \quad (3)$$

where k_B is the Boltzmann constant, μ is the mean molecular weight (taken to be 0.62), m_p is the proton mass, m_i and T_i are the mass and temperature of the ith gas resolution element. The summations are done on all resolution elements within a radial shell centred

on radius r with thickness $\delta r = 0.01 R_{\rm vir}$, in a simulation snapshot corresponding to time t. Finally, the 3D turbulent velocity $\sigma_{\rm turb}$ at radius r and time t is calculated via

$$\sigma_{\rm turb} = \sqrt{\sigma_r^2 + \sigma_\theta^2 + \sigma_\phi^2}, \tag{4}$$

where σ_r, σ_θ, and σ_ϕ are the velocity dispersions in the radial, polar, and azimuthal directions, respectively. The angle θ is defined with respect to the total angular momentum vector of stars within $0.2 R_{\rm vir}$, and ϕ is the corresponding azimuthal angle. To obtain the velocity dispersion in each direction, we calculate the variance of the velocity components as follows:

$$\sigma_j^2 = \overline{(u_j - \langle u_j \rangle_\rho)^2}, \tag{5}$$

where u_j represents the velocity component in the jth direction for an individual resolution element ($j = r, \theta, \phi$), and as above $\langle\rangle_\rho$ indicates a mass-weighted average. Summation is done over all gas resolution elements in a shell centred on radius r with thickness $0.01\ R_{\rm vir}$. Our choice to calculate the dispersion in spherical coordinates avoids contributions to $\sigma_{\rm turb}$ from coherent motions in the radial or rotational directions.

2.5 Cooling time and free-fall time

The formation of a long-lived and quasi-static hot phase occurs when $t_{\rm cool}^{\rm (s)}$, the cooling time of shocked gas at the halo virial temperature ('s' for shocked) exceeds the free-fall time $t_{\rm ff}$ (White & Rees 1978; Birnboim & Dekel 2003; Mo, Chen & Wang 2024). Stern et al. (2020, 2021a) demonstrated that $t_{\rm cool}^{\rm (s)}/t_{\rm ff}$ increases with CGM radius in a given halo, and thus hot phase formation occurs above a higher halo mass threshold of $\approx 10^{12}\,{\rm M}_\odot$ at inner CGM radii than at outer CGM radii (see Introduction). In this work, we focus on this transition in the inner CGM which is expected to occur at $z < 1$ for Milky-Way mass galaxies. We measure $t_{\rm cool}^{\rm (s)}$ and $t_{\rm ff}$ in the FIRE simulations at inner CGM radii as described in Stern et al. (2021a) and summarized here. We calculate $t_{\rm cool}^{\rm (s)}$ at a given radius r via

$$t_{\rm cool}^{\rm (s)} \equiv t_{\rm cool}\left(T^{\rm (s)}\right) = \frac{(3/2)\cdot k_{\rm B} T^{\rm (s)}}{\mu X \langle n_{\rm H}\rangle \Lambda}, \tag{6}$$

where $\langle n_{\rm H}\rangle$ is the volume-weighted average density in a shell with radius r, X is the hydrogen mass fraction, and $T^{\rm (s)}$ is the temperature of a cooling flow in the subsonic limit

$$T^{\rm (s)} = \frac{3}{5}\frac{\mu m_{\rm p} v_{\rm c}^2}{k_{\rm B}} \approx T_{\rm vir} \tag{7}$$

(see equation 24 in Stern et al. 2019). The cooling function Λ is defined such that $n_{\rm H}^2\Lambda$ is the radiative energy loss rate per unit volume and is calculated using the tables in Wiersma, Schaye & Smith (2009), using $T^{\rm (s)}$, Z, $\langle n_{\rm H}\rangle$, and z as input parameters. The free-fall time is calculated as

$$t_{\rm ff} = \frac{\sqrt{2} r}{v_{\rm c}}. \tag{8}$$

Note that since $\Lambda(T)$ decreases roughly as $T^{-0.5}$ at $T \approx 10^6$ K, the ratio $t_{\rm cool}^{\rm (s)}/t_{\rm ff}$ scales strongly with $v_{\rm c}$, as $\sim v_{\rm c}^4$.

3 RESULTS: UV ABSORPTION SIGNATURES OF TURBULENCE-DOMINATED INNER CGM

3.1 UV absorbers trace the volume-filling medium

Fig. 1 plots the temperature distribution and absorption characteristics in the inner CGM of the m12i FIRE simulation, for an example absorption line Si III λ1206. The left column shows the $z = 0$ snapshot after the quasi-static hot phase has formed in the inner CGM ($t_{\rm cool}^{\rm (s)} = 9\, t_{\rm ff}$), while the right snapshots shows $z = 0.75$ (lookback time $t_{\rm lookback} \approx 6.6$ Gyr), before the quasi-static hot phase has formed ($t_{\rm cool}^{\rm (s)} = 0.3\, t_{\rm ff}$). The top row shows temperature maps of the interstellar medium (ISM) and inner CGM in these two snapshots, produced using a mass-weighted projection of $\log T$ in a slice with depth 1 kpc centred on the halo centre. Panel size is $0.4 R_{\rm vir}$ in each axis. Gas velocities relative to the halo centre in the projection plane are overplotted as grey arrows.

In the $z = 0$ snapshot shown on the left of Fig. 1 the temperature map shows a prominent hot, diffuse medium with localized cooler regions, or 'clouds'. In contrast, the $z = 0.75$ snapshot shown on the right reveals a more disordered temperature distribution with widespread cooler regions, as found by previous studies of FIRE simulations (Stern et al. 2021a; Gurvich et al. 2023).

The dashed lines in the top panels represent trajectories of mock sightlines used for analysing UV absorption. The middle panels plot the volume density of Si^{++} ions $n_{\rm Si^{++}}$ along these sightlines, where 0 is defined as the location along the sightline which is nearest to the halo centre. At $z = 0$ after the hot quasi-static phase has formed, $n_{\rm Si^{++}}$ is characterized by isolated peaks, corresponding to localized cool clouds embedded in the hot CGM as in the common paradigm for UV absorbers (e.g. Tumlinson, Peeples & Werk 2017). In contrast, at $z = 0.75$, the Si^{++} density profile is more continuous and widespread along the sightlines, indicating that Si^{++} ions are part of the volume-filling phase rather than limited to localized clouds. We show below that this alternative paradigm, where circumgalactic UV absorbers trace the volume-filling phase, is applicable to all UV ions originating in inner CGM without a quasi-static hot phase.

The bottom panels of Fig. 1 show the absorption spectrum of Si III 1206 Å in the mock sightline, generated with TRIDENT assuming an instrumental spectral resolution of $R = 20\,000$. The absorption line equivalent widths W_λ are noted in each panel. At $z = 0$, the absorption feature is optically thin and relatively weak with $W_\lambda = 0.3$Å, due to the less extensive presence of cool gas. Conversely, at $z = 0.75$, the absorption feature is saturated over a range of $\gtrsim 100\,{\rm km\,s^{-1}}$ with $W_\lambda = 0.97$Å, due to the large amount of cool gas in the inner CGM.

3.2 Wide lognormal gas density distributions

Fig. 2 presents mass-weighted gas density distributions in the two snapshots shown in Fig. 1. We include in the distribution all gas resolution elements within a thin shell with a radius of $0.2\, R_{\rm vir}$, without any selection by gas temperature. This radius is chosen as a representative radius of the inner CGM that is beyond regions where angular momentum support is dominant (typically $\lesssim 0.05\, R_{\rm vir}$, see Stern et al. 2021a). Shell thickness is chosen to be $\delta r = 0.01 R_{\rm vir}$ in order to avoid the range in density induced by radial gradients. The colour indicates the average $\log T$ of gas at each density, while the thin curves plot lognormal fits to the density distributions, defined via

$${\rm PDF}(\log\rho) = \frac{1}{\sqrt{2\pi}\sigma_{\log\rho}} \exp\left(-\frac{\left(\log\rho - \mu_{\log\rho}\right)^2}{2\sigma_{\log\rho}^2}\right), \tag{9}$$

where ρ is the density, $\mu_{\log\rho}$ is the mean of $\log\rho$, and $\sigma_{\log\rho}$ is the standard deviation of $\log\rho$. Here and henceforth we use log as shorthand for $\log_{10}$.

At $z = 0$, the density distribution shown in the top panel of Fig. 2 has a Gaussian-like shape with $\sigma_{\log\rho} \approx 0.21$ dex and an asymmetric tail extending towards higher densities. The Gaussian

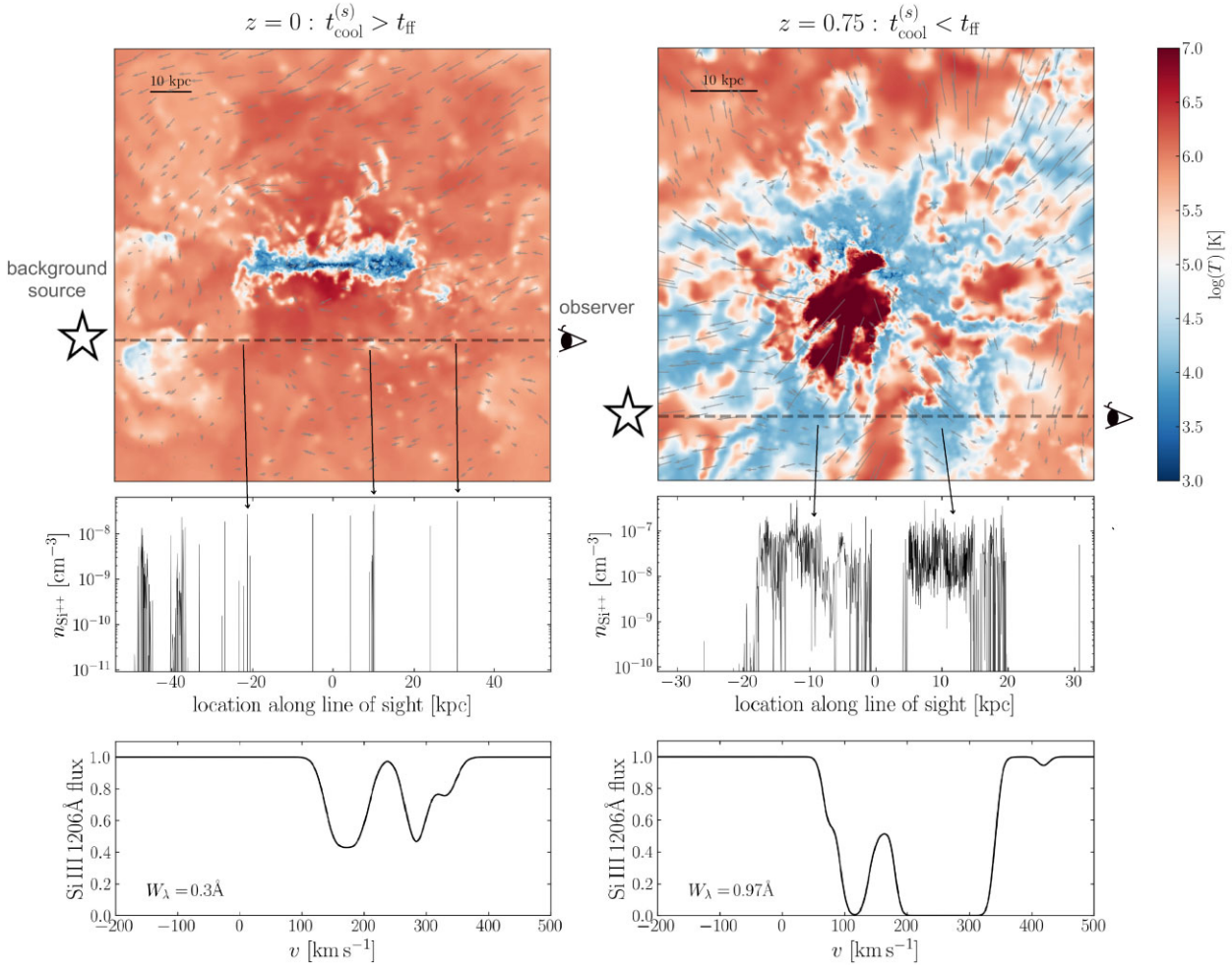

Figure 1. A qualitative difference between UV absorbers before and after a quasi-static hot phase forms in the CGM. Columns show two snapshots of a Milky Way-mass galaxy simulated in FIRE ('m12i'). Left panels show the $z = 0$ snapshot where hot gas cools slowly so the inner halo is filled with a quasi-static hot phase, while right panels show the $z = 0.75$ snapshot where hot gas cools rapidly so the hot phase is limited to localized and transient clouds. Top panels show gas temperature maps extending to $0.2R_{\rm vir}$ and the trajectories of mock sightlines through them (dashed lines). Middle panels show Si^{++} volume density along the mock sightlines, with 0 kpc defined as the location nearest to the halo centre, and arrows connecting cool gas in the images with peaks in $n_{\rm Si^{++}}$. Bottom panels show predicted Si III absorption spectra for spectral resolution $\lambda/\Delta\lambda = 20\,000$. At $z = 0$, Si III traces localized cool clouds embedded in a hot $T \approx T_{\rm vir}$ medium, consistent with the common paradigm for UV absorbers. In contrast at $z = 0.75$ Si III traces the cool volume filling phase of the inner CGM.

is dominated by temperatures of $\gtrsim 10^6$ K, while the tail has lower temperatures of 10^4–10^5 K. This distribution demonstrates that the gas is predominantly in a hot diffuse phase with some cooler regions of higher density, as indicated also by Fig. 1 and consistent with the common 'multiphase' paradigm of the CGM.

At $z = 0.75$, the density distribution shown in the bottom panel of Fig. 2 is substantially broader and more symmetric than at $z = 0$. A lognormal distribution with $\sigma_{\log\rho} \approx 0.72$ dex provides a reasonable fit to the entire distribution, regardless of gas temperature. Most of the gas is cool, with ≈ 74 per cent of the mass having $T < 3 \cdot 10^4$ K. The hot $T > 10^{5.5}$ K gas accounts only for ≈ 14 per cent of the total gas mass and 58 per cent of the volume. The origin of this wide lognormal distribution, which is distinct from the hot peak + cool tail distribution shown in the top panel, is further discussed below.

The hot phase being subdominant at $r = 0.2\,R_{\rm vir}$ in the $z = 0.75$ snapshot is a result of the short cooling time ($t_{\rm cool}^{(s)} < t_{\rm ff}$) at this redshift and radius, which implies that any hot gas formed via accretion or feedback shocks rapidly cools (Stern et al. 2021a). This is in contrast with cases where $t_{\rm cool}^{(s)} > t_{\rm ff}$ and hence the hot shocked gas is long-lived, such as the $z = 0$ snapshot at $r = 0.2\,R_{\rm vir}$ (the top panel of Fig. 2) and the $z = 0.75$ snapshot at a larger CGM radius of $r = 0.5\,R_{\rm vir}$, shown in Appendix A.

The evolution of hot gas mass fraction in the inner CGM is further explored in the top panel of Fig. 3, which plots the mass fraction in each CGM phase versus $t_{\rm lookback}$. Blue shows the cool phase with temperatures $T < 3 \cdot 10^4$ K, red shows the hot phase with temperatures $T > 3 \cdot 10^5$ K, and intermediate temperatures are shown in black. As in Fig. 2, we sum only gas resolution elements within a thin shell centred at $0.2\,R_{\rm vir}$, to avoid the effects of radial gradients. Each data point represents an individual snapshot from the simulation, while the lines and shaded regions indicate the average values and their dispersions within a window spanning 25 snapshots (≈ 600 Myr). The top axis plots the corresponding redshift. There is a marked increase in the mass fraction of the hot gas phase at $2 \lesssim t_{\rm lookback} \lesssim 5$ Gyr. This is the formation of the quasi-static hot phase in the inner CGM as noted by previous FIRE studies, and is coincident with $t_{\rm cool}^{(s)}$ exceeding $t_{\rm ff}$ (Stern et al. 2021a; Gurvich et al. 2023).

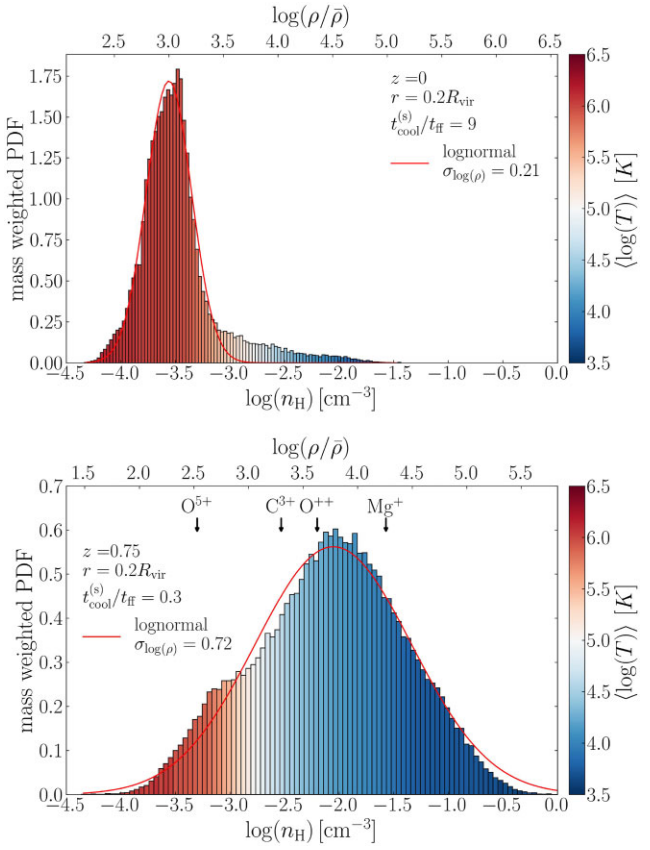

Figure 2. Density distribution of gas in a thin shell with $r = 0.2R_{\rm vir}$, for the two snapshots shown in Fig. 1. Colour indicates the mean temperature at each density, and the top axes denote the density in units of the cosmic mean. The ratio of hot gas cooling time to free-fall time is noted in the panels. At $z = 0$ (top), the distribution is narrow with $\sigma_{\log\rho} = 0.21$ and a tail towards high densities, as expected in the common CGM paradigm with a low-density hot phase and denser cool clouds. Conversely, at $z = 0.75$ (bottom) the gas is predominantly cool and the distribution is a broad lognormal with $\sigma_{\log\rho} = 0.72$, as expected in isothermal turbulent gas with Mach ~ 10. Labels denote the median density of gas which produces each ion.

Note that the mode of the density distributions in Fig. 2 shifts from $n_{\rm H} \approx 10^{-3.5}\,{\rm cm}^{-3}$ at $z = 0$ to $n_{\rm H} \approx 10^{-2}\,{\rm cm}^{-3}$ at $z = 0.75$. This shift to higher density at higher redshift is partially due to the increase in mean cosmic density. In units of the cosmic mean $\bar{\rho} = 3\Omega_b H^2/8\pi G$ the mode is $\rho/\bar{\rho} = 5 \cdot 10^3$ at $z = 0.75$, compared to $\rho/\bar{\rho} = 10^3$ at $z = 0$ (see top-axes of Fig. 2). The remaining difference arises from our choice to weigh the density distribution by mass. The volume-weighted mean density, i.e. the total shell mass divided by its volume, are similar in the two snapshots in units of $\bar{\rho}$.

3.3 Supersonic turbulence

The middle panel of Fig. 3 shows the evolution of different velocity components at $0.2\,R_{\rm vir}$, calculated according to equations (2)–(4): turbulent velocity (green), circular velocity (red), and mass-weighted sound speed (black). At early times the mass-weighted sound speed is less than $50\,{\rm km\,s^{-1}}$ due to the dominance of cool $\sim 10^4$ K gas as seen in the top panel. The turbulent velocity is $\approx 150\,{\rm km\,s^{-1}}$ and comparable to $v_{\rm c}$ especially at early times, indicating the CGM is dominated by turbulence. This result demonstrates that $\sigma_{\rm turb}$ significantly exceeds the mass-weighted sound speed, i.e. CGM

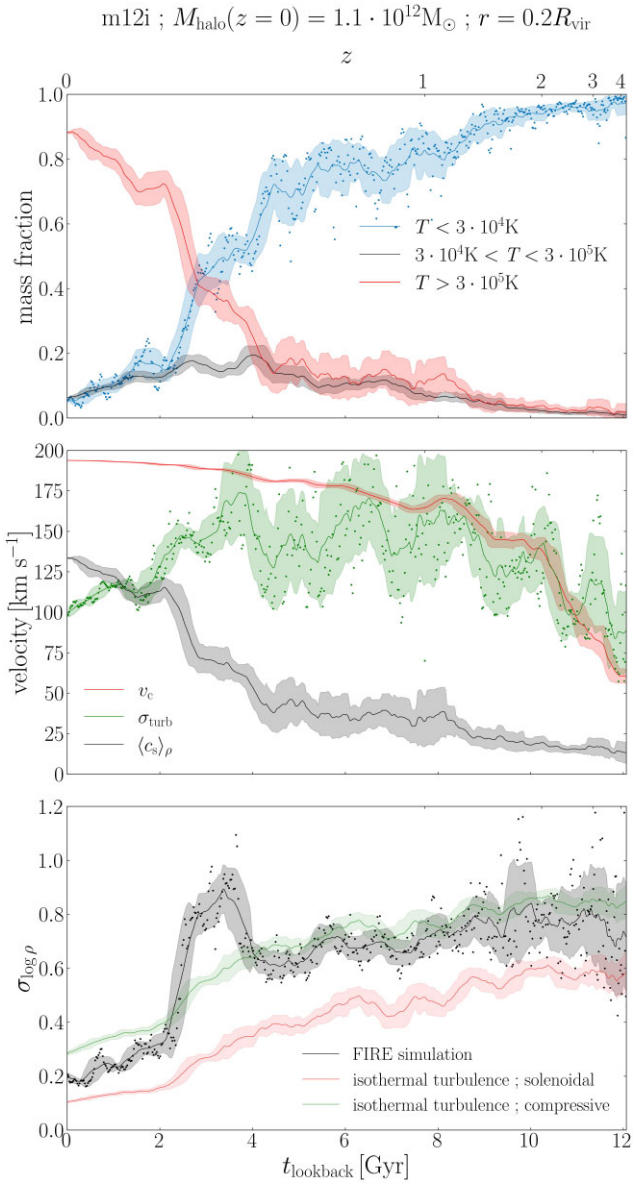

Figure 3. Top: Evolution of mass fractions of gas with different temperatures at $r = 0.2\,R_{\rm vir}$ in the m12i simulation. Dots denote individual snapshots (shown only for cool gas for clarity), while lines and bands denote means and dispersions within a running 600 Myr window. The mass fraction of hot gas (red) sharply increases after $t_{\rm lookback} \approx 4$ Gyr. Middle: Evolution of 3D turbulent velocity (green), circular velocity (red), and mass-weighted sound speed (black) at $0.2\,R_{\rm vir}$. CGM turbulence is highly supersonic when the cool phase dominates. Bottom: Black dots and line denote the width of the density distribution at $0.2\,R_{\rm vir}$, derived using a lognormal fit to the distribution in each snapshot (see Fig. 2). Red lines indicate the expected $\sigma_{\log\rho}$ based on isothermal turbulence simulations with two types of driving mechanisms and the same Mach number as in FIRE (equations 10 and 11). A wide density distribution is apparent when turbulence is supersonic (> 4 Gyr) consistent with isothermal turbulence simulations with compressive driving.

turbulence is supersonic. When the hot phase becomes dominant at $t_{\rm lookback} \lesssim 2$ Gyr the mass-weighted sound speed rises above $100\,{\rm km\,s^{-1}}$, while the turbulent velocity declines from $\approx 150\,{\rm km\,s^{-1}}$ to $100\,{\rm km\,s^{-1}}$. The formation of the hot quasi-static phase thus corresponds to turbulent velocities dropping below the mean sound speed, i.e. the turbulences become subsonic.

Idealized simulations of isothermal turbulence demonstrate that the width of the density distribution increases with turbulent Mach number, roughly as (e.g. Krumholz 2014)

$$\sigma_s^2 = \ln\left(1 + b_t^2 \mathcal{M}_{\rm turb}^2\right) \ , \tag{10}$$

where $\sigma_s = 0.43\,\sigma_{\log\rho}$ is the width of the lognormal density distribution for a natural logarithm, $\mathcal{M}_{\rm turb}$ is the turbulent Mach number and b_t is a unit-less parameter which equals ≈ 1 for pure compressive turbulence driving and $\approx 1/3$ for pure solenoidal driving.[2] We check here whether equation (10) can explain the density distribution in the CGM of the non-isothermal FIRE simulations.

The bottom panel of Fig. 3 plots the evolution of $\sigma_{\log\rho}$ versus $t_{\rm lookback}$, derived by fitting the density distribution at $0.2\,R_{\rm vir}$ in each snapshot with a lognormal as done in Fig. 2. Before the formation of the hot phase when turbulent velocities are larger than the mean sound speed we find $\sigma_{\log\rho} \approx 0.6$–$0.8$, as shown for the $z = 0.75$ snapshot in the bottom panel of Fig. 2. This dispersion is significantly larger than after the hot phase forms where the value of $\sigma_{\log\rho} \approx 0.2$–$0.3$, as shown for the $z = 0$ snapshot in the top panel of Fig. 2. At the transition itself $\sigma_{\log\rho}$ is highest with values of $0.8 - 1.0$, since both the cold and hot gas mass fractions are ≈ 50 per cent and hence the density dispersion spans both phases, i.e. a unimodal fit is no longer justified.

To compare the density distribution in FIRE with that predicted by isothermal turbulence simulations we measure the following average turbulent Mach number in the simulations:

$$\tilde{\mathcal{M}}_{\rm turb} \equiv \frac{\sigma_{\rm turb}}{\langle c_s \rangle_\rho} \ . \tag{11}$$

The bottom panel of Fig. 3 plots the expected $\sigma_{\log\rho}(\tilde{\mathcal{M}}_{\rm turb})$ based on equation (10) for $b_t = 1/3$ and $b_t = 1$. The panel shows that equation (10) reasonably captures the relation between turbulence Mach number and the density distribution, both at early times when the cold phase dominates and at late times when the hot phase dominates. The similarity is best for compressive driving ($b_t = 1$) mainly at the early supersonic stage, though note that this conclusion may be affected by our choice of how to average c_s for the calculation of $\tilde{\mathcal{M}}_{\rm turb}$. Only during the transition from cool phase dominance to hot phase dominance at $t_{\rm lookback} \approx 3$ Gyr the value of $\sigma_{\log\rho}$ is significantly larger than expected based on isothermal simulations, since the width spans both peaks of a bi-modal density distribution.

The similarity between FIRE and isothermal turbulence simulations shown in the bottom panel of Fig. 3 suggests that (1) at a given radius, the density dispersion in the dominant CGM phase is set by turbulence physics; and (2) the formation of a quasi-static hot phase causes a transition in the nature of CGM turbulence, from supersonic turbulence with wide density distributions pre-ICV, to subsonic CGM turbulence with narrow density distributions post-ICV.

Fig. 4 shows the evolution of the ratio of turbulent pressure ($P_{\rm turb}$) to the total pressure ($P_{\rm turb} + P_{\rm thermal}$) in the same simulation (m12i), calculated as

$$\frac{P_{\rm turb}}{P_{\rm turb} + P_{\rm thermal}} = \frac{\frac{1}{3}\sigma_{\rm turb}^2}{\frac{1}{3}\sigma_{\rm turb}^2 + \frac{3}{5}\langle c_s \rangle_\rho^2} \ . \tag{12}$$

where the factor of $1/3$ is because we defined $\sigma_{\rm turb}$ as the 3D velocity dispersion (equation 4). The ratio is calculated at two different radial distances: $r = 0.2R_{\rm vir}$ (black) and $r = 0.5R_{\rm vir}$ (red). For $r = 0.2R_{\rm vir}$, the ratio remains relatively constant and high until $t_{\rm lookback} \approx 4$ Gyr, after which there is a rapid decline, as suggested by Fig. 3. At $r = 0.5R_{\rm vir}$, the ratio starts at a lower value and decreases more gradually over time, without a sharp transition. The ratio remains lower than at $r = 0.2R_{\rm vir}$ until the hot phase forms at $t_{\rm lookback} \approx 2$ Gyr, reflecting the higher importance of thermal pressure and longer $t_{\rm cool}^{\rm (s)}$ at larger radii, consistent with previous results (Stern et al. 2021a; Gurvich et al. 2023).

[2]The subscript 't' differentiates b_t from absorption line width b used below.

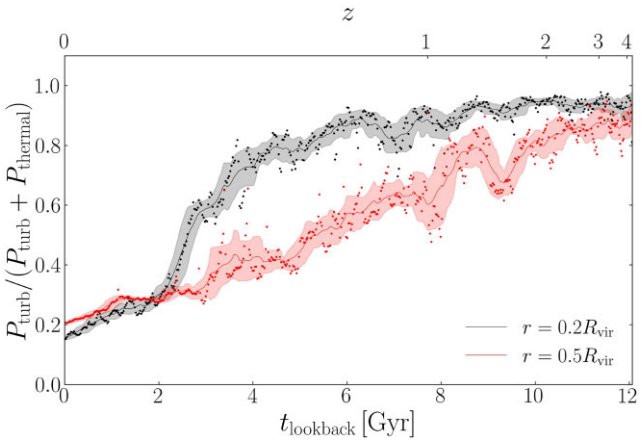

Figure 4. Evolution of the ratio of turbulent pressure ($P_{\rm turb}$) to total pressure ($P_{\rm turb} + P_{\rm thermal}$) in the CGM of the FIRE m12i simulation. Different colours denote gas at $r = 0.2R_{\rm vir}$ (black) and at $r = 0.5R_{\rm vir}$ (red). Dots represent individual data points, while lines and shaded bands represent running averages and dispersions within a 600 Myr window. The inner CGM exhibits a relatively sharp transition (within ≈ 2 Gyr) between turbulent pressure dominance to thermal pressure dominance, corresponding to the formation of a quasi-static hot phase in the inner CGM as seen in Fig. 3. At larger radii the importance of turbulence decreases more gradually with time.

3.4 Equivalent widths of $\sim$ 1Å in strong UV transitions

In Figs 1–3, we showed that most of the inner CGM is cool prior to the formation of a quasi-static hot phase, with a turbulent velocity of order 150 km s^{-1} and a wide density distribution of $\sigma_{\log\rho} \approx 0.7$ dex at a given radius. In this section we demonstrate that these properties imply high equivalent widths of ~ 1 Å for commonly observed UV absorption features.

3.4.1 Analytic estimate of equivalent widths

We first estimate the absorption equivalent width W_λ in inner CGM dominated by turbulence analytically, by assuming saturated absorption in strong transitions due to the near-unity mass fraction of cool gas. In saturated absorbers the equivalent width is determined by the velocity range of the absorption, which in turn is set by the turbulent velocity. We thus get a rough estimate of the equivalent width of

$$W_\lambda \sim \frac{2b}{c}\lambda \approx \sqrt{\frac{8}{3}}\frac{\sigma_{\rm turb}}{c}\lambda = 1.0\text{Å} \cdot \left(\frac{\sigma_{\rm turb}}{150\,{\rm km\,s^{-1}}}\right)\left(\frac{\lambda}{1206\text{Å}}\right) \ , \tag{13}$$

where b is the absorption line width, equal to $\sqrt{2}$ times the line-of-sight velocity dispersion so $b \approx \sqrt{2/3}\sigma_{\rm turb}$, and λ is the wavelength of the transition normalized to that of Si III. We thus expect $W_\lambda \sim 1$Å in UV absorption features which originate in inner CGM dominated by turbulence.

To demonstrate that strong UV absorption lines are indeed saturated in turbulence-dominated CGM, we use the equation for optical

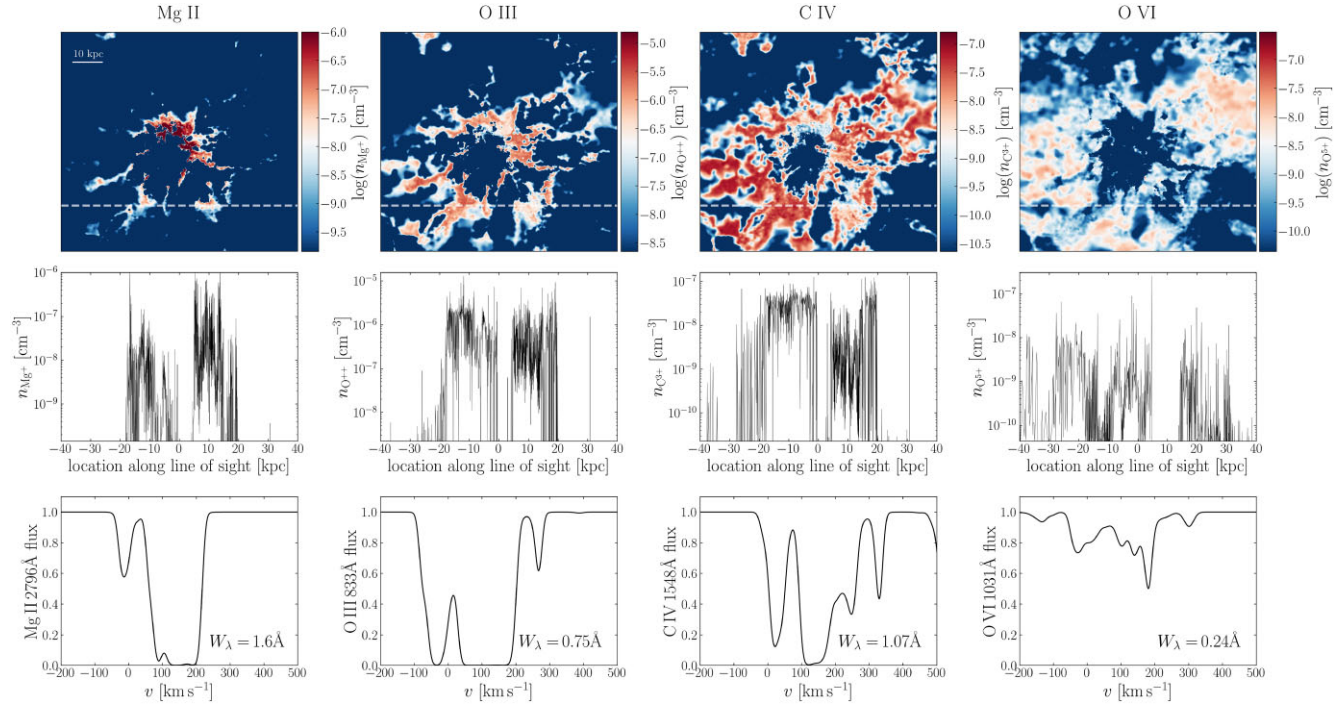

Figure 5. Top row: Maps of ion volume density in the turbulence-dominated $z = 0.75$ snapshot shown in Figs 1–2, for Mg^+ (left), O^{++} (middle left), C^{3+} (middle right), and O^{5+} (right). Middle row: Ion density as a function of location along the mock sightline marked as a dashed line in the top panels. Bottom row: Absorption spectra for the three ions assuming $R = 20\,000$. Equivalent widths are noted in the panels. All ions shown are spread over a significant fraction of the line of sight, indicating that collectively they trace the volume-filling phase of the inner CGM, rather than tracing localized clouds and interfaces with a hot phase as usually assumed. Mg II traces the high density part of the lognormal density distribution shown in Fig. 2, and thus appears at the highest density peaks. O III and C IV originate from the centre of the distribution and are thus widespread, while O VI traces the low density part of the density distribution.

depth at line centre (e.g. Draine 2011):

$$\tau = 0.015 \frac{\mathrm{cm}^2}{\mathrm{s}} \cdot \frac{N_{\rm ion} \lambda f_{\rm lu}}{b} = \approx 5.8 \left(\frac{N_{\rm H}}{10^{20.5}\,\mathrm{cm}^{-2}}\right) \left(\frac{f_{\rm lu}\frac{N_{\rm X}}{N_{\rm H}}}{10^{-5}}\right) \left(\frac{f_{\rm ion}}{0.1}\right) \left(\frac{\lambda}{1206\text{Å}}\right) \left(\frac{150\frac{\mathrm{km}}{\mathrm{s}}}{\sigma_{\rm turb}}\right) \quad (14)$$

where $N_{\rm ion} = N_{\rm H}(N_{\rm X}/N_{\rm ion}) f_{\rm ion}$ is the ion column (see equation 1), and the total hydrogen column density $N_{\rm H}$ is normalized by typical CGM values (e.g. equation B6 in Stern et al. 2021b):

$$N_{\rm H} = 7 \cdot 10^{20} f_{\rm CGM} M_{12}^{1/3} \left(\frac{1+z}{2}\right)^2 \left(\frac{R_\perp}{0.2\,R_{\rm vir}}\right)^{-1} \mathrm{cm}^{-2}, \quad (15)$$

where $f_{\rm CGM}$ is the CGM mass in units of the halo baryon budget, assumed to be 0.5 for the estimate in equation (14). The product $f_{\rm lu} \cdot N_{\rm X}/N_{\rm ion}$ in equation (14) is normalized by 10^{-5}, characteristic of strong UV absorbers assuming $Z = 0.3\,Z_\odot$ (Table 2). The estimate of $f_{\rm ion} \sim 0.1$ is based on the result that the CGM is predominantly cool and has a broad range of gas densities at each radius during the turbulence-dominated stage, spanning a factor of ≈ 50 (full width at half-maximum, FWHM) in the example shown in the bottom panel of Fig. 2. Since the ionization state in photoionized cool gas depends on the ratio of ionizing photon density to gas density, this broad range in density implies that many UV-absorbing ions have optimal formation conditions in a significant fraction of the gas along the sightline (say, $\gtrsim 10$ per cent), and we thus expect $f_{\rm ion} \gtrsim 0.1$ for these ions. The broad range in density implies also that the predicted $f_{\rm ion}$ are robust to the factor of ≈ 2 uncertainty in the ionizing photon density (see Section 2.3). Taken together, these considerations indicate that strong UV transitions have $\tau \gg 1$, i.e. highly saturated absorption features as assumed in the estimate of W_λ in equation (13).

How does the predicted W_λ depend on $M_{\rm halo}$ and z for fixed $R_\perp/R_{\rm vir}$? We show below that $\sigma_{\rm turb} \approx v_{\rm c}$ in CGM dominated by turbulence. We thus expect W_λ to scale roughly as $v_{\rm c} \propto M_{\rm halo}^{1/3}$ for fixed z and as $v_{\rm c} \propto (1+z)^{0.5}$ for fixed halo mass. Different halo masses and redshifts can also change the predicted τ, though this will significantly change W_λ only if the transition becomes optically thin.

3.4.2 *Equivalent widths in FIRE*

Fig. 5 shows the spatial distributions and absorption characteristics of Mg^+, O^{++}, C^{3+}, and O^{5+}, in the $z = 0.75$ snapshot of m12i shown above. The top row maps the ion volume densities in a 1 kpc-thick slice, while the middle row shows the ion volume densities along the mock sightline (plotted as dashed lines in the top panels). The maps show that the filling fractions of the ions increase from Mg^+ to O^{++} to C^{3+}, where Mg^+ has the most intermittent structure while C^{3+} has a more continuous and widespread distribution. O^{5+} has a similar filling fraction and pattern as C^{3+} except at inner radii where it is absent.

The different spatial distributions of the different ions shown in Fig. 5 are a result of higher ions generally tracing lower densities (which imply higher photoionization) and higher temperatures (which imply higher collisional ionization). The different densities correspond to different parts of the wide gas density distribution in supersonically turbulent CGM. Specifically, the mass-weighted density and temperature of Mg^+ along the mock sightline are $0.03\,\mathrm{cm}^{-3}$ and $0.9 \cdot 10^4$ K with a 16–84 density percentile range

of 0.02–0.1cm^{-3}, corresponding to the high-density part of the log-normal density distribution shown in the bottom panel of Fig. 2. For O^{++}, the corresponding density and temperature are $6 \cdot 10^{-3}$ cm^{-3} and $1.4 \cdot 10^4$ K, while for C^{3+} we find $3 \cdot 10^{-3}$ cm^{-3} and $2.6 \cdot 10^4$ K. These two ions thus trace gas densities near the peak of the density distribution. For O^{5+} the mass-weighted density and temperature along the sightline are $5 \cdot 10^{-4}$ cm^{-3} and $2 \cdot 10^5$ K, i.e. this ion traces the low-density part of the density distribution shown in Fig. 2.

The spatial distributions of different ions shown in Fig. 5 demonstrate the volume-filling nature of UV-absorbing gas during the turbulence-dominated phase, where different ions trace different parts of a broad density distribution which is predominantly cool. This is a qualitatively distinct picture from the common paradigm where low-ion UV absorbers trace 'localized clouds' and mid-ions trace interfaces between the clouds and the hot background.

The bottom panels in Fig. 5 plot the absorption spectra for Mg II 2796Å, O III 833Å, C IV 1548Å, and O VI 1031Å. Except for O VI, these absorption features and that of Si III 1206Å (the bottom-right panel of Fig. 1) indeed exhibit a velocity spread of $\approx$ 100–200 km s^{-1} and $W_\lambda \sim 1$Å, as expected based on the analytic estimate in equation (13). The corresponding values of $f_{\rm ion}$ along the sightline are 0.29, 0.17, and 0.24 for Mg^+, O^{++}, and Si^{++}, respectively, consistent with the order of magnitude estimate of $f_{\rm ion} \sim 0.1$ in the previous section. For C^{3+} we find a lower $f_{\rm ion} = 0.008$, and the optical depth is close to unity. For O VI we find $f_{\rm ion} = 10^{-3}$ and thus the transition is optically thin with $W_\lambda = 0.24$ Å. The relatively low optical depth and W_λ of O VI are a result of this ion tracing densities which are two standard deviations below the peak of the lognormal distribution, and thus such gas densities are relatively scarce.

The absorption profiles shown in the plot are limited to contributions from $\pm$60 kpc along the sightline. We verified that the contribution from larger scales to the absorption is small. For example W_λ(O VI) increases from 0.24 to 0.3 Å when accounting for scales up to $\pm$500 kpc, comparable to the size of the region fully simulated by the zoom simulation.

Fig. 6 plots the evolution of W_λ versus lookback time. Each panel presents a different ion at two impact parameters ($0.2R_{\rm vir}$ in black and $0.5R_{\rm vir}$ in red), where dots indicate individual mock sightlines (five per snapshot), while lines and bands denote averages and dispersions in running windows spanning 600 Myr. Before the transition at $t_{\rm lookback} > 5$ Gyr we find $W_\lambda \approx 1$Å at $0.2\,R_{\rm vir}$ for all three ions shown, as expected from the analytic estimate in equation (13). At $t_{\rm lookback} \lesssim 2$, Gyr after the hot phase becomes dominant W_λ drops in all ions since cool gas is less abundant (see Fig. 3). After the transition W_λ also differs between different ions and evolves with time, in contrast with the approximately uniform W_λ prior to the transition.

At $R_\perp = 0.5\,R_{\rm vir}$ the values of W_λ shown in Fig. 6 are consistently lower than at $R_\perp = 0.2\,R_{\rm vir}$, especially for Mg II, and exhibit a more gradual decline with time. This reflects both the dominance of the hot phase in the outer CGM, and the overall lower gas columns and lower gas densities at larger radii (see Fig. A1 and Stern et al. 2021a).

Fig. 7 plots the evolution of the mean W_λ for all strong UV and EUV transitions listed in Table 2. At $t_{\rm lookback} > 4$ Gyr when the inner CGM is turbulence dominated we find $\langle W_\lambda \rangle \sim 0.2$–2 Å in all shown absorption features except for O VI where $\langle W_\lambda \rangle \approx 0.02$–0.1 Å. In contrast after $t_{\rm lookback} < 2$ Gyr when the hot phase has formed the values of $\langle W_\lambda \rangle$ are substantially lower, in the range 10^{-3}–0.2 Å.

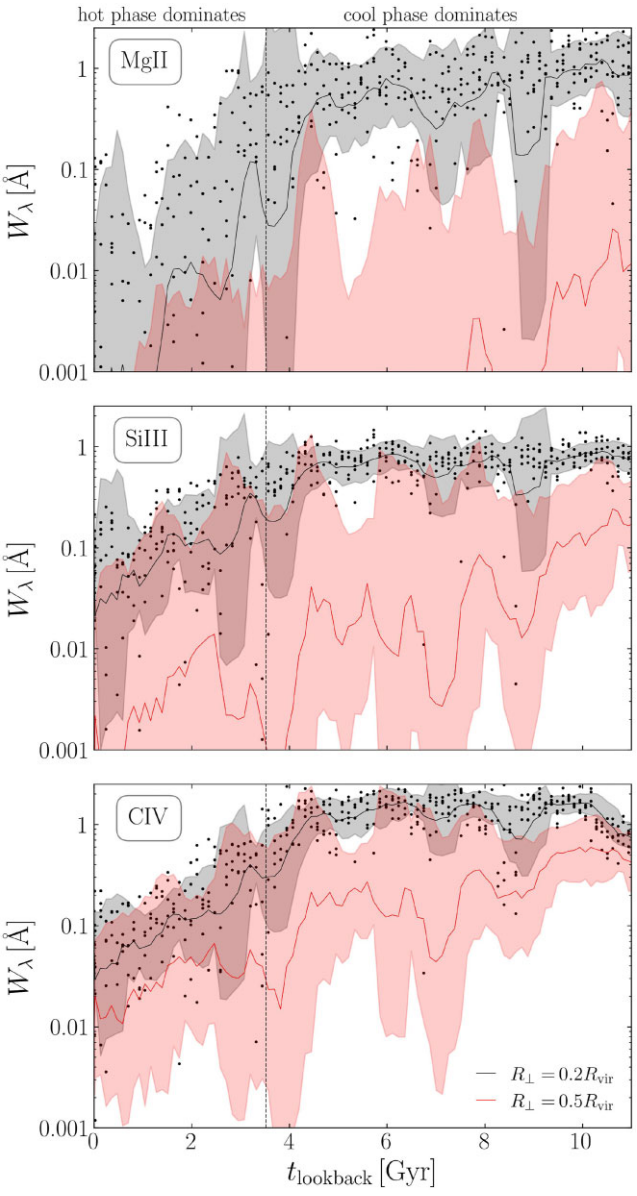

Figure 6. Predicted evolution of CGM absorption equivalent widths in m12i. Different panels show different ions, while impact parameters are denoted by colour. Dots represent individual mock sightlines (shown for $R_\perp = 0.2\,R_{\rm vir}$), while lines and bands represent averages and dispersions within a running 600 Myr window. Vertical lines denote the time after which the hot phase dominates (see Fig. 3). At $t_{\rm lookback} > 4$ Gyr when the cool phase dominates we predict $W_\lambda(0.2\,R_{\rm vir}) \approx 1$Å in all ions, consistent with the analytic approximation (equation 13). After the hot phase forms $W_\lambda(0.2\,R_{\rm vir}) \ll 1$Å.

3.5 Dependence on halo mass history

In this subsection, we explore how the mass history of the halo affects the transition from turbulence-dominated CGM to thermal-pressure dominated CGM and the implied absorption signatures.

Fig. 8 repeats the analysis in Fig. 3 for three simulations: a group-size halo (m13A1, left panels), another Milky Way-mass galaxy halo (m12b, middle panels), and a dwarf galaxy halo (m11d, left panels). In the massive m13A1 simulation, the hot phase becomes dominant, and the turbulence becomes subsonic at an early time

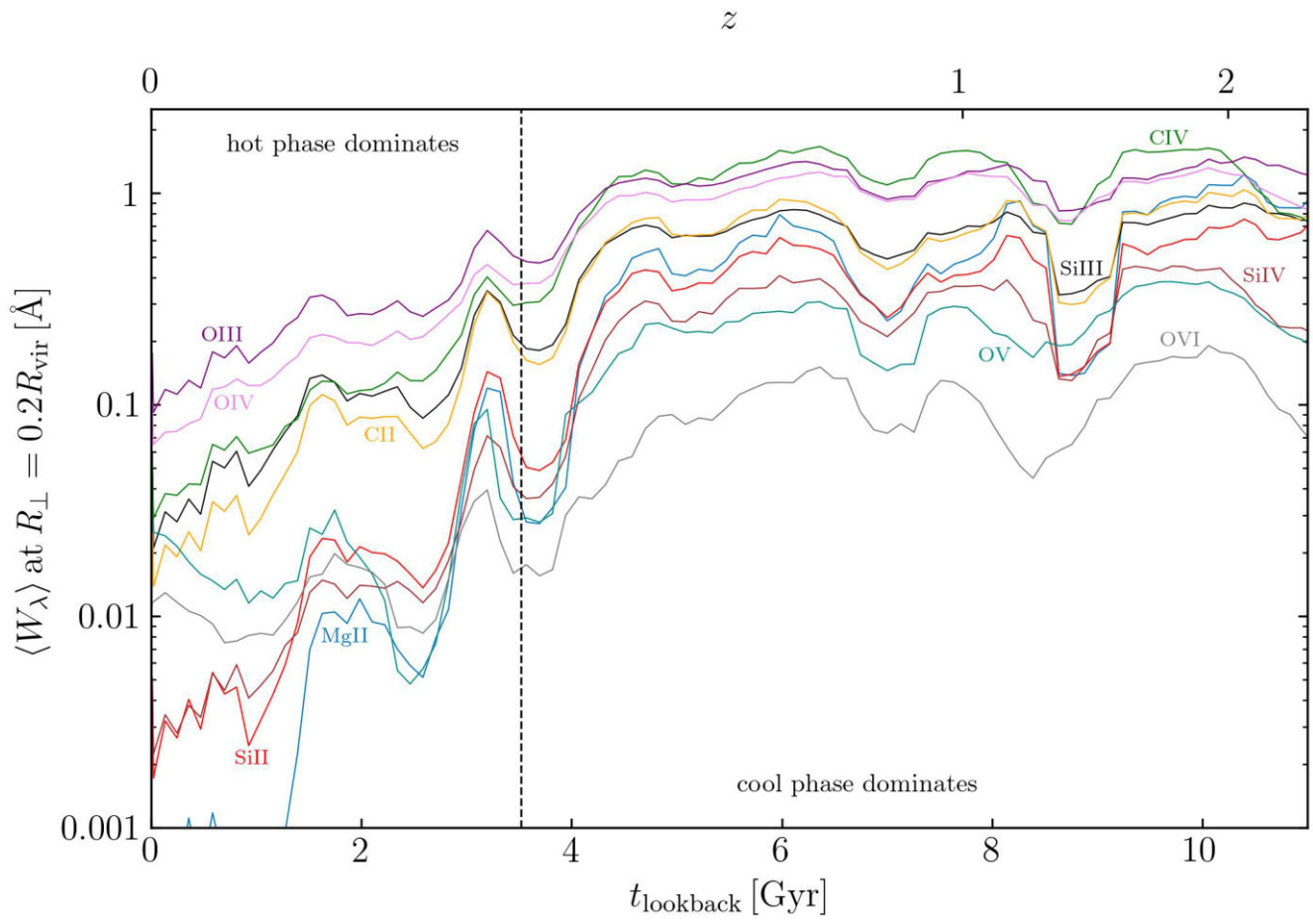

Figure 7. Predicted evolution of mean absorption equivalent widths of UV absorption features at an impact parameter of $0.2R_{\rm vir}$, based on the m12i simulation. Absorption features are listed in Table 2, while plotted lines are labelled by the respective ions. The vertical dashed line indicates when the hot phase becomes dominant by mass. Before this transition cool gas and turbulence dominate and $W_\lambda \sim 1$Å is predicted for most plotted features, while afterwards W_λ drops.

of $t_{\rm lookback} \approx 11.5$ Gyr ($z \approx 3.2$). This follows since $t_{\rm cool}^{\rm (s)}$ exceeds $t_{\rm ff}$ earlier in more massive haloes (Stern et al. 2021a). In the m12b simulation shown in the middle column, the hot phase becomes dominant by mass and the turbulence becomes subsonic at $t_{\rm lookback} \approx 6$ Gyr ($z \approx 0.65$), a few Gyr before the transition occurs in m12i (see Fig. 3). This demonstrates the range in formation times of the inner hot CGM phase in Milky-Way mass FIRE galaxies, which typically span $0 < z < 1$ (see Stern et al. 2021a, and below). The m12b simulation also exhibits a bump in the cool gas mass fraction at $t_{\rm lookback} \approx 2$ Gyr after the hot gas formed, coincident with a major merger occurring at this time as noted by Yu et al. (2021). In the dwarf galaxy halo shown in the left column the cool gas phase dominates the mass at all times. Correspondingly, the turbulent velocity remains higher than the mean sound speed, i.e. turbulent velocities remain supersonic. This result reflects the Stern et al. (2021a) result that a quasi-static hot CGM phase does not form in the inner CGM of FIRE dwarfs, since $t_{\rm cool}^{\rm (s)}$ remains lower than $t_{\rm ff}$ down to $z = 0$.

Fig. 9 plots the evolution of $\langle W_\lambda \rangle$ for various strong UV transitions in the three simulations, similar to the analysis of m12i in Fig. 7. In m13A1 (top panel), a clear drop in mean W_λ occurs already around $t_{\rm lookback} = 11.5$ Gyr, consistent with the early transition to a thermal energy-dominated inner CGM phase in this simulation. Equivalent widths of the Mg II, C II, Si II, Si III, and O III transitions are 1–3 Å prior to the transition, somewhat higher than the $\langle W_\lambda \rangle \approx 0.7$–1 Å in m12i prior to the transition. The higher W_λ are due to the higher turbulent velocity of 200–300 km s^{-1} (the bottom-left panel of Fig. 8) and hence higher b in more massive haloes (see equation 13). In contrast, the O IV, C IV, and Si IV have lower W_λ of 0.1–0.3 Å, likely due to the weak UV background (relative to typical CGM density) at $z \gtrsim 3$, which implies that cool photoionized gas does not reach high ionization levels.

The CGM of m12b shown in the middle panel of Fig. 9 exhibits similar UV absorption figures as m12i (shown in Fig. 6), albeit the transition happens earlier at $t_{\rm lookback} \approx 7$ Gyr consistent with the earlier formation of a quasi-static hot inner CGM phase in this simulation. As in m12i, $\langle W_\lambda \rangle \approx 0.3$–1 Å prior to ICV in most absorption lines while O VI has a lower $\langle W_\lambda \rangle \approx 0.1$–0.2 Å. The values of $\langle W_\lambda \rangle$ for all ions drop following ICV.

The dwarf galaxy halo shown in the bottom panel of Fig. 9 exhibits $\langle W_\lambda \rangle \approx 0.1$–0.7 Å down to $z = 0$, again with the exception of O VI which has a lower $\langle W_\lambda \rangle \approx 0.03$ Å. As mentioned above this halo remains in the turbulence-dominated stage at all times. These W_λ are somewhat lower than the $W_\lambda \sim 0.2$–2 Å in m12i and m12b during their turbulent-dominated stage. The difference is mainly a result of the lower turbulent velocities of ≈ 70 km s^{-1} in m11d (the bottom-right panel of Fig. 8), which results in narrower absorption features and thus lower W_λ (see equation 13).

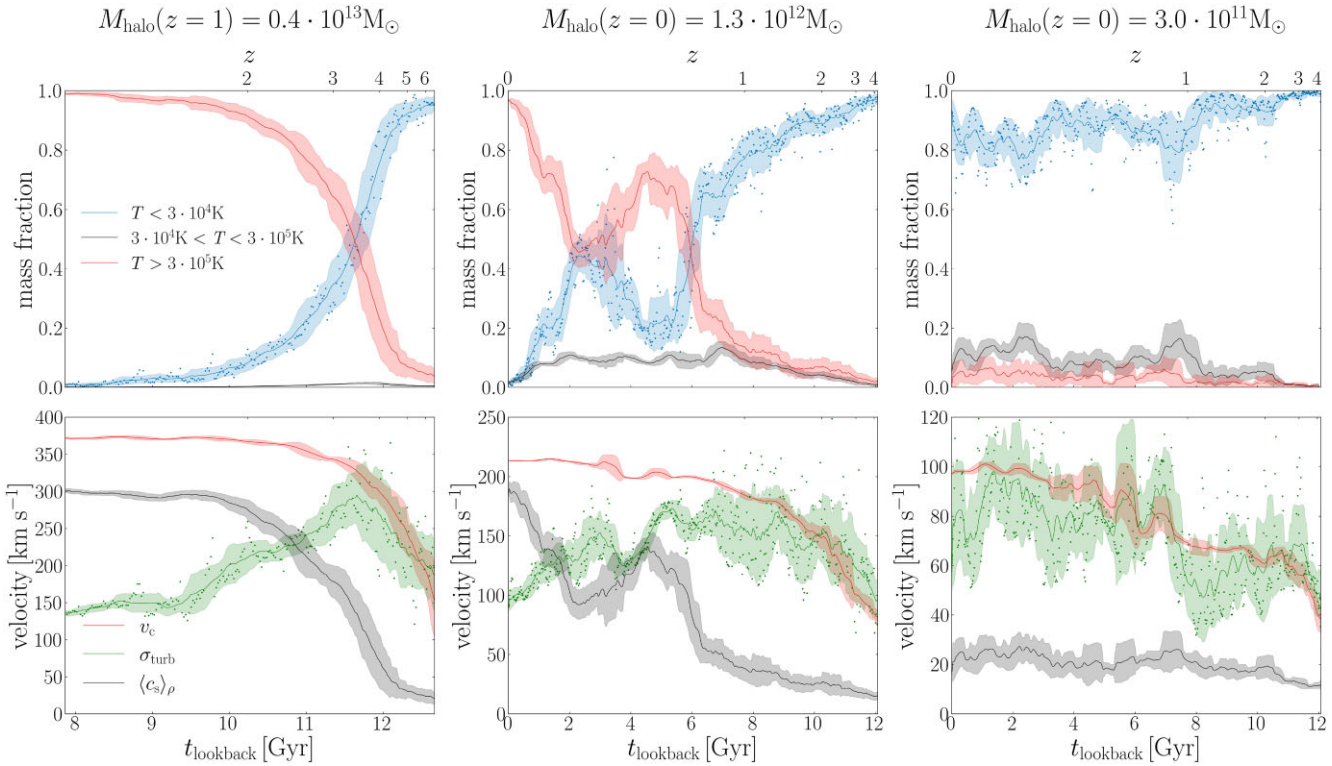

Figure 8. Top: Evolution of the mass fractions of different CGM phases at $r = 0.2R_{\rm vir}$, in three FIRE simulations of haloes of different masses. The panels from left to right correspond to a group-size halo ('m13A1'), a Milky Way-mass galaxy ('m12b'), and a dwarf galaxy ('m11d'). Dots represent individual snapshots (shown only for the cool phase for clarity), while lines and bands represent averages and dispersions within a running 600 Myr window. Bottom: Evolution of the turbulent velocity (green), circular velocity (red), and mass-weighted sound speed (black) at $r = 0.2R_{\rm vir}$. Note the difference in plotted velocity ranges between the panels. A significant increase in hot gas mass fraction is apparent around $t_{\rm lookback} \approx 7$ Gyr in m12b and $t_{\rm lookback} \approx 12$ Gyr in m13A1, indicating the formation of a quasi-static hot phase with subsonic turbulence. The short-term decrease in hot gas mass fraction in m12b at $t_{\rm lookback} \approx 2$ Gyr is associated with a major merger. The m11d galaxy on the right remains dominated by the supersonically turbulent cool phase at all times.

3.6 Dependence on resolution

To test how our results depend on simulation resolution, we repeat the analysis for two additional simulations of the m12i halo with eight times higher/lower gas mass resolution than in the fiducial simulation (see Table 1). The results are shown in Fig. B1 in the appendix. The top two rows are similar to the two top panels of Fig. 3, while the bottom row shows the mean equivalent width of Mg II and the ratio $t_{\rm cool}^{\rm (s)}/t_{\rm ff}$ measured at $0.1R_{\rm vir}$ (equations 6 and 8). The figure shows that v_c increases somewhat more slowly at higher resolution, and thus $t_{\rm cool}^{\rm (s)}/t_{\rm ff}$ which scales as $\sim v_c^4$ (see Section 2.5) exceeds unity later, as also found by Stern et al. (2021a). At all shown resolutions we find that prior to ICV when $t_{\rm cool}^{\rm (s)} < t_{\rm ff}$, the cool gas mass fraction is > 50 per cent, turbulence is on average supersonic ($\sigma_{\rm turb} > \langle c_s \rangle_\rho$), and the equivalent width of Mg II is $\gtrsim 1$ Å. This suggests that the conditions for the development of turbulence-dominated CGM and their predicted equivalent widths are independent of resolution at the range probed. This lack of sensitivity to resolution is because turbulence-dominated CGM are predominantly cool even at low resolution.

At $z = 0$ when the inner CGM is dominated by thermal pressure, Fig. B1 shows that $f_{\rm cool}$ increases with increasing resolution, consistent with the conclusion of previous studies (Hummels et al. 2019; Peeples et al. 2019; van de Voort et al. 2019; Ramesh & Nelson 2024). However, it is not clear if the increasing $f_{\rm cool}$ in FIRE is a direct result of the increasing resolution, or rather a result of the lower $t_{\rm cool}^{\rm (s)}/t_{\rm ff}$ at higher resolution which produces a higher $f_{\rm cool}$.

4 COMPARISON WITH UV ABSORPTION OBSERVATIONS

A common paradigm for circumgalactic UV absorbers is that the absorption originates from a cool 'cloud', or from the interface between a cool cloud and the ambient hot medium (e.g. Tumlinson et al. 2017; Faucher-Giguère & Oh 2023). Our results suggest an alternative origin for $W_\lambda \sim 1$Å absorbers, in which they trace the volume-filling medium of the inner CGM, in haloes with $t_{\rm cool}^{\rm (s)} < t_{\rm ff}$ where the inner CGM is predominantly cool and supersonically turbulent.

In this section, we compare this alternative paradigm for $W_\lambda \sim 1$Å absorbers with several observational constraints. This allows us to infer which types of galaxies in the real universe have a turbulence-dominated inner CGM rather than a thermal energy-dominated inner CGM, and thus constrain how the formation of a thermal-energy dominated inner CGM affects galaxy evolution.

4.1 Mg II equivalent widths

The Mg II absorption doublet is observable from the ground at $z \gtrsim 0.1$ (e.g. Chen et al. 2010; Nielsen, Churchill & Kacprzak 2013; Werk et al. 2013), and thus has been the subject of a large number of circumgalactic UV absorption surveys at the redshifts we focus on in this paper ($0 \leq z \lesssim 2$). Fig. 10 compares observed mean rest-frame equivalent widths $\langle W_{\rm MgII} \rangle \equiv \langle W_{2796} + W_{2803} \rangle$ at impact parameters of $R_\perp = 0.2\,R_{\rm vir}$ to those predicted by the FIRE simulations. We

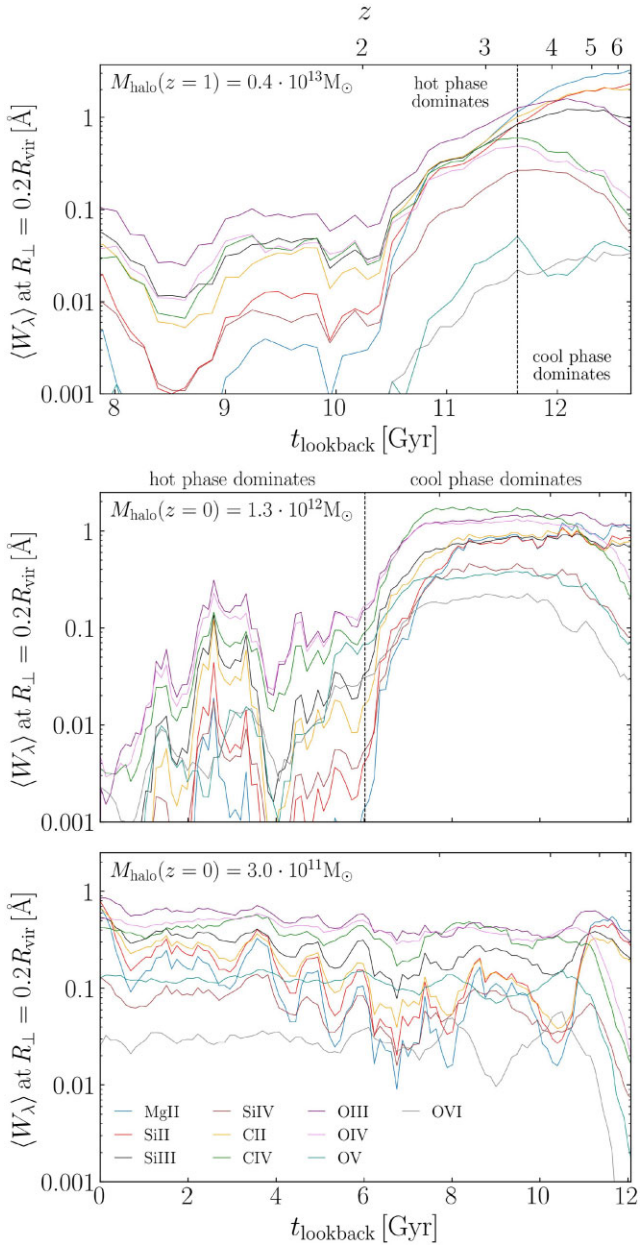

Figure 9. Evolution of mean W_λ at $R_\perp = 0.2R_{\rm vir}$ for the three simulations shown in Fig. 8. The dashed vertical lines indicate the transition from an inner CGM dominated by cool gas and turbulence to an inner CGM dominated by the hot phase. Equivalent widths are high (≈ 1 Å) before the transition and decrease afterward. The lowest-mass halo shown in the bottom panel remains cool and turbulent at all times, with $0.1 < W_\lambda < 1$ Å for all ions except O VI.

focus on average values since some of the observed $\langle W_{\rm MgII} \rangle$ are measured on stacked spectra, though we note that the predicted dispersion between sightlines is not large during the turbulence-dominated phase, of order ≈ 0.3 dex (see Fig. 6). Predictions of the five m12 FIRE simulations are shown as solid coloured lines, where $\langle W_{\rm MgII} \rangle$ are calculated over 200 mock sightlines within 1200 Myr running windows (five sightlines per snapshot). We use larger windows than above in order to reduce clutter in the figure. Times when the inner CGM is dominated by cool gas ($f_{\rm cool} > 0.5$) are emphasized with thicker lines. A drop in the predicted $\langle W_{\rm MgII} \rangle$ is evident when the inner CGM becomes thermal pressure-dominated at $3 < t_{\rm lookback} < 6$ Gyr ($0.25 < z < 0.6$) in four of the haloes (m12i, m12b, m12c, m12f). The fifth halo m12w does not show a drop in $\langle W_{\rm MgII} \rangle$ despite reaching $f_{\rm cool} = 0.5$ at $t_{\rm lookback} = 3$ Gyr, likely since it remains with $f_{\rm cool} \approx 0.5$ and $t_{\rm cool}^{\rm (s)} \approx t_{\rm ff}$ down to $z = 0$, i.e. it does not fully transition to thermal-energy dominated regime. This is potentially due to its somewhat lower halo mass than the other m12's and the strong dependence of $t_{\rm cool}^{\rm (s)}/t_{\rm ff}$ on halo mass (see Stern et al. 2021a, and Table 1).

During times when turbulence dominates, all five simulations predict similar $\langle W_{\rm MgII} \rangle$, as expected based on the analytic arguments in Section 3.4.1. We fit the predictions in these pre-ICV snapshots with a log-linear relation:

$$\log \frac{\langle W_{\rm Mg\,II} \rangle_{\rm pre-ICV}}{\text{Å}} = -0.31 + 0.05 \, \frac{t_{\rm lookback}}{\rm Gyr} \, . \tag{16}$$

This relation is consistent with the order of magnitude analytic estimate of $\langle W_{\rm MII} \rangle_{\rm pre-ICV} \sim 1$ Å in equation (13) and is plotted as a dotted line in Fig. 10. The main prediction of this paper is that $\sim L^*$ galaxies roughly follow this relation as long as the energetics of their inner CGM remains dominated by turbulence.

Observed $\langle W_{\rm Mg\,II} \rangle$ at $R_\perp = 0.2\,R_{\rm vir}$ from blue $\sim L^\star$ galaxies are plotted as errorbars in Fig. 10 and listed in Table 3. Most observational surveys shown are based on matching background sources with foreground galaxies, such that each foreground galaxy has a single sightline through its CGM. The exceptions are the measurements based on gravitational arcs which have multiple sightlines through a single foreground galaxy, since the background source is a lensed galaxy. To derive $\langle W_{\rm Mg\,II} \rangle (R_\perp = 0.2 R_{\rm vir})$ we interpolate the $\langle W_{\rm MgII} \rangle$ versus $R_\perp / R_{\rm vir}$ relation deduced in each survey. The horizontal error bar spans the redshift range of the sample, with the marker located at the median redshift. Blue galaxy samples with mean stellar $M_\star > 10^{10}\,{\rm M}_\odot$ are considered $\sim L^\star$ and plotted in the figure. Additional details on this calculation for each survey are given in Appendix C.

Fig. 10 demonstrates that the observed $\langle W_{\rm MgII} \rangle$ of SF $\sim L^\star$ galaxies at $R_\perp = 0.2 R_{\rm vir}$ is $\gtrsim 1$Å at $0.1 \lesssim z \lesssim 1.5$. These observed values are consistent with the predictions of turbulence-dominated inner CGM (dotted line, equation 16) to within a factor of ≈ 2. We emphasize that since turbulence-dominated CGM make specific predictions for UV absorption strength (Section 3.4.1), this match between predictions and observations is highly non-trivial. We thus conclude that turbulence-dominated CGM correctly predict $\langle W_{\rm MgII} \rangle$ observed in inner CGM surrounding blue $\sim L^*$ galaxies.

The blue galaxy observations shown in Fig. 10 do not show a drop in $\langle W_{\rm MgII} \rangle$ at low redshift similar to that predicted by the four m12 simulations in which ICV occurs. Rather, the observations more resemble the m12w simulation which predicts only a mild decrease in $\langle W_{\rm Mg\,II} \rangle$ with redshift since it remains with $f_{\rm cool} \gtrsim 0.5$ down to $z = 0$. This difference is potentially due to the somewhat lower masses in the $\sim L^\star$ observations than in the m12 simulations, since when and if ICV occurs strongly depends on mass. A simulation sample better matched in mass to the observations could test this possibility.

The drop in $\langle W_{\rm Mg\,II} \rangle$ exhibited by four of the m12 simulations predicts that the most massive blue galaxies at low redshift should exhibit $\langle W_{\rm Mg\,II} \rangle (0.2\,R_{\rm vir}) \ll 1$Å, due to their thermal pressure-dominated inner CGM, in contrast with the blue $\sim L^\star$ galaxies observed by the surveys shown in Fig. 10. Tentative evidence for this distinction is seen in fig. 4 of Lan (2020), where the most massive galaxy bin at $0.4 < z < 0.7$ has $\langle W_{\rm Mg\,II} \rangle (0.2\,R_{\rm vir}) \ll 1$Å. Additional support for this comes from the low Si II and C IV columns observed in the CGM of the Milky Way and M31, as discussed below.

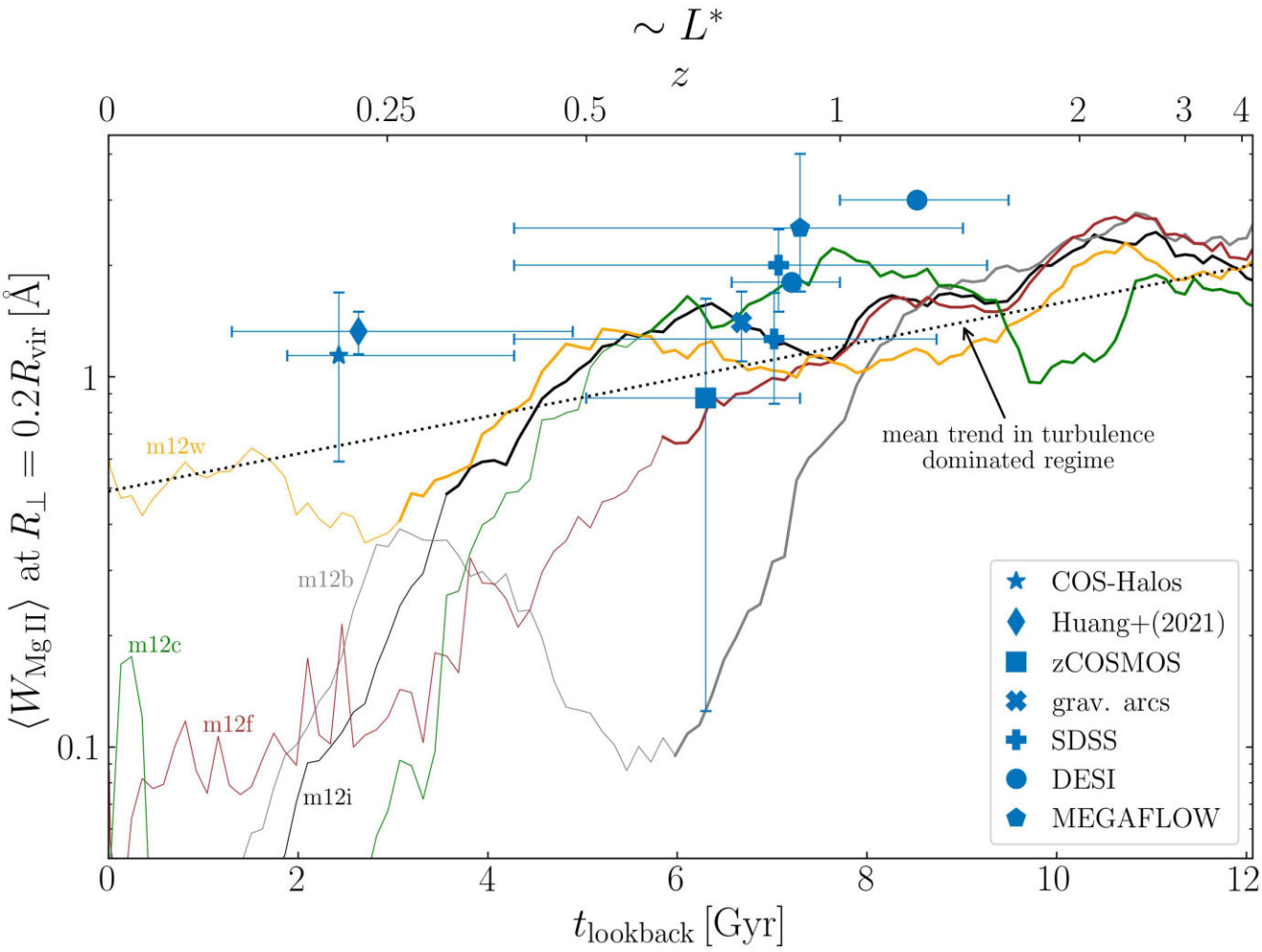

Figure 10. Observed Mg II absorption at $R_\perp = 0.2R_{\rm vir}$ from blue $\sim L^\star$ galaxies versus FIRE predictions. Solid coloured lines show the evolution of the mean Mg II equivalent width $\langle W_{2796} + W_{2803}\rangle$ in five simulated $\sim L^\star$ galaxies. Thicker segments of each curve indicate pre-ICV ($f_{\rm cool} > 0.5$, turbulence-dominated) times, and the dotted black line shows the mean trend in this regime. Thin segments show post-ICV ($f_{\rm cool} < 0.5$, thermally supported) times which in most cases predict substantially lower $\langle W_{\rm Mg\,II}\rangle$. Observed values from the blue $\sim L^\star$ surveys listed in Table 3 are plotted as markers and errorbars. Observed $\langle W_{\rm Mg\,II}\rangle$ at $R_\perp = 0.2\,R_{\rm vir}$ in SF $\sim L^\star$ galaxies are consistent with the predictions of turbulence-dominated inner CGM to a factor of ≈ 2.

Fig. 11 compares the FIRE predictions for $\langle W_{\rm Mg\,II}\rangle$ with observations of blue dwarf galaxies ($M_\star < 10^{10}\,{\rm M}_\odot$) and luminous red galaxies (LRGs), also listed in Table 3. The inner CGM in the m11d simulation shown in the left panel remains cool and turbulent at all times as discussed above. The predicted $\langle W_{\rm Mg\,II}\rangle$ at $0.2R_{\rm vir}$ largely remains within the range 0.3–1 Å consistent with the observed values. The predicted $\langle W_{\rm Mg\,II}\rangle$ in m13A1 shown in the right panel drops at early times, as expected given the early ICV in this massive simulation. The mean observed values of the LRG samples are also $\ll 1$ Å, inconsistent with the predictions of turbulent-dominated inner CGM. Fig. 11 thus suggests that the inner CGM of blue dwarf galaxies are turbulent dominated, while the inner CGM of LRGs are thermal-energy dominated, as expected.

The difference in predicted Mg II absorption between turbulence-dominated and thermal energy-dominated inner CGM is also evident in Fig. 12, which plots W_{2796} versus impact parameter at $t_{\rm lookback} = 2$ Gyr ($z = 0.15$) and at $t_{\rm lookback} = 5$ Gyr ($z = 0.5$) in the m12i simulation, corresponding to just after and just before ICV. We plot the mean and scatter of W_{2796} from five consecutive snapshots centred on each of these two times, using ten sightlines per 0.025 dex-wide bin in $R_\perp$, and then smoothing the curve with a Savitzky–Golay filter to reduce clutter. The panel shows that at $z = 0.5$ when turbulence dominates high equivalent widths of a few tenths of Å extend into the inner CGM, in contrast with being limited to disc radii ($< 0.1R_{\rm vir}$) at $z = 0.15$ when thermal energy dominates. The observed W_{2796} from blue $\sim L^\star$ galaxies in the COS-Haloes and Huang et al. (2021) samples shown in the left panel exhibit high W_{2796} at inner CGM radii consistent with the turbulence-dominated regime, albeit with a larger dispersion. This difference is potentially due to the range in mass and redshift spanned by the observations in contrast with the single galaxy and redshift in the FIRE predictions shown in Fig. 12.

The right panel of Fig. 12 is similar to the left panel, but showing observations from red galaxies in the COS-haloes and Huang et al. (2021) samples. Red galaxies exhibit on average lower W_{2796} than blue galaxies at inner CGM radii, with approximately two-thirds of sightlines at 0.1–0.3$R_{\rm vir}$ having $W_{2796} < 0.2$ Å, in contrast with only 15 per cent of sightlines in the blue galaxy sample. High W_{2796} absorbers thus exist around red galaxies but are not ubiquitous as they are around blue galaxies, ruling out a cool phase-dominated turbulent inner CGM for red galaxies. The $\approx 1/3$ of sightlines with high equivalent widths around red galaxies are not predicted by the

Table 3. Details of circumgalactic $\langle W_{\rm Mg\,II}\rangle$ measurements shown in Figs 10 and 11. Columns: (1) survey name; (2) mean stellar mass; (3) mean halo mass, derived from mean $M_\star$, mean z, and the $M_{\rm halo} - M_\star$ relation in Behroozi et al. (2019); (4) mass group of foreground galaxies (dwarf, $\sim L^*$ or LRG); (5) foreground galaxy type (SF: star-forming, Q: quiescent); (6) sample redshift range; (7) sample median redshift; (8) impact parameter equal to 0.2 $R_{\rm vir}$; (9) measured mean Mg II equivalent width; (10) reference paper. See additional details in Appendix C.

Survey (1)	log $M_\star$ ($M_\odot$) (2)	log $M_{\rm halo}$ ($M_\odot$) (3)	Mass group (4)	Type (5)	$z_{\rm range}$ (6)	$\langle z\rangle$ (7)	$R_\perp$ (kpc) (8)	$\langle W_{\rm MgII}\rangle$ (Å) (9)	Ref. (10)
zCOSMOS	9.6	11.5	Dwarf	SF	0.5–0.9	0.7	25	0.5 ± 0.1	Bordoloi et al. (2011)
	10.2	11.9	L^*	SF			33	0.9 ± 0.75	
	10.9	13.0	LRG	Q			81	0.2 ± 0.6	
COS-Haloes	10.3	11.9	L^*	SF	0.15–0.4	0.2	46	1.14 ± 0.55	Werk et al. (2013)
SDSS	10.5	12.2	L^*	SF	0.4–1.5	0.85	39	2.0 ± 0.5	Lan & Mo (2018)
	10.4	12.1	L^*	SF	0.4–1.3	0.84	36	1.27 ± 0.42	Anand et al. (2021)
	11.2	13.5	LRG	Q	0.4–0.7	0.55	124	0.15 ± 0.05	Lan & Mo (2018)
	11.5	14.0	LRG	Q	0.4–0.6	0.54	183	<0.4	Anand et al. (2021)
DESI	10.0	11.8	L^*	SF	0.75–1.0	0.88	28	1.8 ± 0.0	Wu et al. (2025)
	10.1	11.8			1.0–1.6	1.23	24	3.0 ± 0.0	
Huang+'21	10.3	11.9	L^*	SF	0.1–0.5	0.22	47	1.2 ± 0.1	Huang et al. (2021)
Gravitational Arcs	9.7	11.7	Dwarf	SF	–	0.73	25	0.6 ± 0.3	Lopez et al. (2020)
	10.1	11.9	L^*	SF	–	0.77	27	1.4 ± 0.3	Mortensen et al. (2021)
MEGAFLOW	10.1	11.8	L^*	SF	0.4–1.4	0.9	26	2.5 ± 1.15	Cherrey et al. (2025)

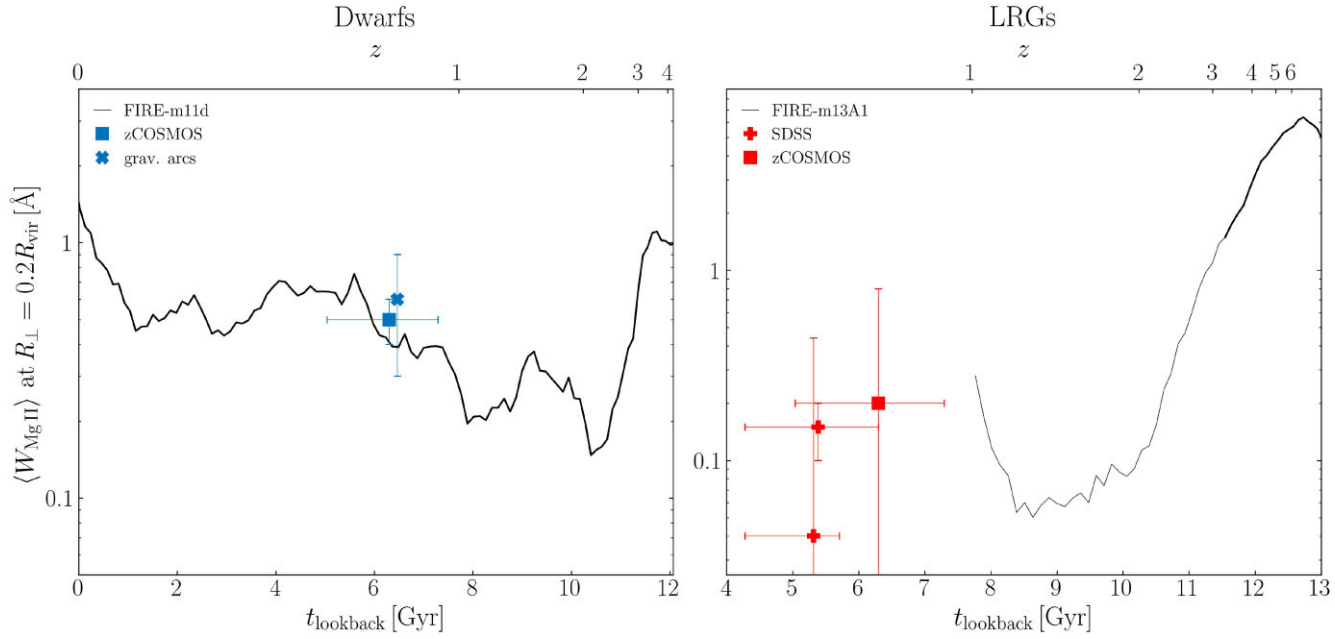

Figure 11. Observed Mg II absorption in dwarf galaxies (left) and in LRGs (right) versus FIRE predictions. Solid lines show predicted $\langle W_{2796+2803}\rangle$ at $R_\perp = 0.2R_{\rm vir}$, with thicker segments corresponding to pre-ICV ($f_{\rm cool} > 0.5$, turbulence-dominated) times. m11d remains turbulence-dominated down to $z = 0$. Observed values from the surveys listed in Table 3 are plotted as markers and errorbars, with marker colour indicating SF (blue) or quiescent (red) galaxies. Blue dwarf galaxy samples are consistent with a turbulence-dominated inner CGM, while LRG observations suggest thermally supported inner CGM.

thermal-dominated FURE snapshot shown in Fig. 12, potentially since localized cool clouds are unresolved in the simulation during the post-ICV stage (see Section 3.6).

4.2 C IV equivalent widths

The FIRE simulations predict a mean $W_{1548} \sim 1$ Å from turbulence-dominated inner CGM of $\sim L^\star$ galaxies (Figs 7 and 9). For comparison, Garza et al. (2025) recently found a mean $W_{1548} = 1 \pm 0.16$ Å in SF COS-haloes galaxies at $R_\perp < 0.3R_{\rm vir}$, compared with a lower mean $W_{1548} = 0.2 \pm 0.08$ Å in quiescent galaxies. C IV absorbers with $W_{1548} > 0.7$ Å are also observed with > 50 per cent covering factor out to $R_\perp = 23^{+62}_{-16}$ kpc around [O II]-emitting galaxies observed with Multi Unit Spectrograph Explorer (MUSE) at $z \sim 1.2$ (Schroetter et al. 2021). This corresponds to an impact parameter of $0.17^{+0.52}_{-0.12}R_{\rm vir}$ for the characteristic $z = 1.2$ and $M_\star = 10^{10}\,M_\odot$ in the Schroetter et al. sample assuming the stellar to halo mass relation from Behroozi et al. (2019). Observed $\langle W_{1548}\rangle$ of SF galaxies are thus also consistent with turbulence-dominated inner CGM, as found above for observations of $\langle W_{\rm MgII}\rangle$.

In lower-mass dwarfs, mean W_{1548} of 0.4 Å are predicted at $z = 0$ (bottom panel of Fig. 9). These values are lower than in more massive turbulence-dominated inner CGM due to the lower turbulent velocities (the bottom-right panel of Fig. 8). For compari-

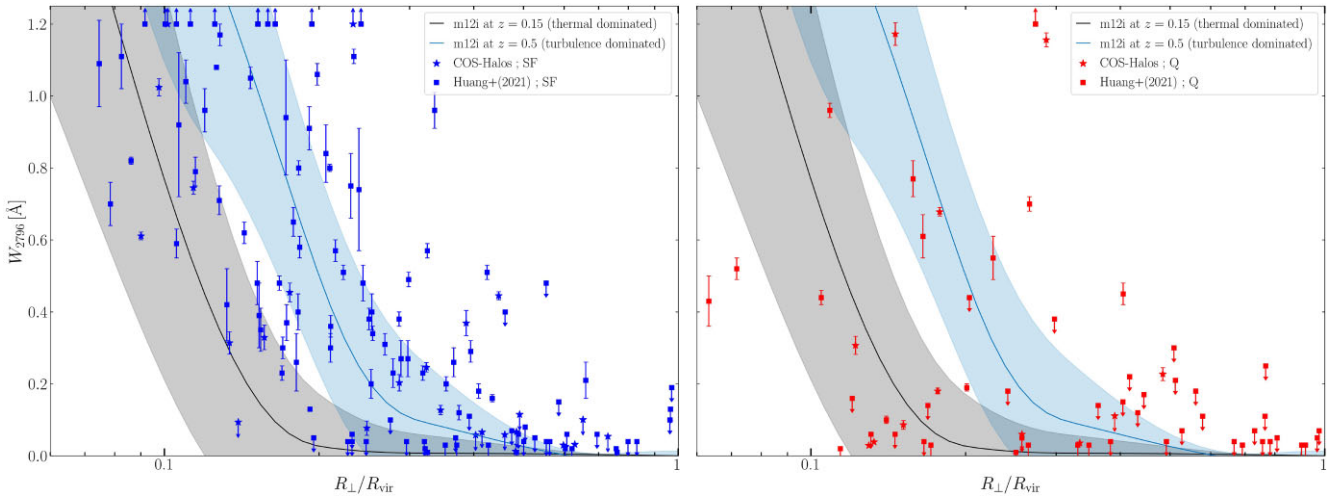

Figure 12. The difference in predicted Mg II equivalent width between turbulence-dominated and thermal energy-dominated inner CGM, versus impact parameter. Solid lines and shaded regions represent the mean and scatter of sightlines through the $z = 0.5$ snapshot (blue, turbulence-dominated) and the $z = 0.15$ snapshot (black, thermally supported) of the m12i simulation. Equivalent widths of a few tenths of Å are predicted from the inner CGM when it is turbulence dominated, while such values are limited to disc radii when the inner CGM is thermally supported. Markers represent observed W_{2796} around SF (left panel) and quiescent (right) galaxies. The ubiquity of high W_{2796} in the inner CGM of SF galaxies supports the turbulence-dominated scenario for these objects.

son, Bordoloi et al. (2014) measured a mean $W_{1548} = 0.45 \pm 0.1$ Å at $0.1 < R_\perp < 0.3\,R_{\rm vir}$ around $z \sim 0.1$ SF dwarf galaxies. Similar values were found at small impact parameter in the samples of Liang & Chen (2014), Johnson et al. (2017), and Manuwal et al. (2021). Observed low-mass blue galaxies are thus consistent with having a cool and turbulent inner CGM, as previously mentioned by Li et al. (2021) and similar to more massive blue galaxies.

The observed prevalence of $W_{1548} \sim 1$ Å in the inner CGM of blue galaxies at $0 < z < 1$ is in contrast with the absence of similar absorbers in the inner CGM of red galaxies (Garza et al. 2025, and see also Bordoloi et al. 2014). This dichotomy is also evident in Mg II absorption as discussed in the previous section. Our results thus suggest that the distinction in inner CGM absorption properties of blue and red galaxies is a manifestation of the difference between a cool, turbulence-dominated inner CGM around blue galaxies, versus a hot, thermal energy-dominated inner CGM around red galaxies. If this interpretation is correct, this distinction should manifest in the $t_{\rm cool}^{\rm (s)}/t_{\rm ff}$ ratio inferred for the CGM of these galaxies, as further discussed in Section 4.4.

We note also that C IV absorption in the inner CGM of the Milky-Way appears to be significantly lower than that in external blue $\lesssim L^*$ galaxies. Bish et al. (2021) deduced a covering fraction of only 20 per cent for $W_{1548} > 0.2$ Å absorbers in the Milky-Way CGM, using sightlines to galactic stars with small angular separations from background quasars in order to account for absorption by the ISM. Such low covering fraction is inconsistent with the turbulence-dominated inner CGM scenario, suggesting that the Milky-Way inner CGM is dominated by a quasi-static hot phase, as suggested also by X-ray observations (see Introduction section). The Bish et al. (2021) results thus suggest that the Milky-Way is post-ICV similar to the m12 simulations at $z = 0$, and in contrast with typical blue $\sim L^\star$ galaxies in the samples shown in Fig. 10.

4.3 Other UV transitions

In the COS-Haloes sample, observations with small impact parameters from blue galaxies and high $\langle W_{\rm MgII}\rangle$ also typically have strong saturated absorption in other transitions, including O VI, Si III, C II, C III, and Si II (Werk et al. 2013; Stern et al. 2016). This implies that such absorbers span a large range in ionization, qualitatively consistent with the wide density and temperature distribution expected in turbulence-dominated inner CGM (bottom panel of Fig. 2). We leave a more quantitative test of the turbulence-dominated CGM regime against the full range of observed absorbers to future work (see Section 5.2).

Lehner et al. (2025) recently found that M31 exhibits $5-6$ times lower Si II columns than those in blue COS-haloes galaxies at $R_\perp < 0.3R_{\rm vir}$, confirming earlier conclusions from Lehner et al. (2020) with better statistics. UV absorption from the inner CGM of M31 thus appears inconsistent with the turbulence-dominated scenario in contrast with blue COS-haloes galaxies, and suggests M31 is post-ICV similar to our m12 simulations at $z = 0$, and as expected since M31 is a massive disc that most likely has a quasi-static hot CGM.

4.4 The $t_{\rm cool}^{\rm (s)} < t_{\rm ff}$ ratio in systems with $\langle W_{\rm Mg\,II}\rangle \sim 1$ Å

Inner CGM filled with a turbulent cool phase are expected when $t_{\rm cool}^{\rm (s)} < t_{\rm ff}$. We demonstrate in this section that this time-scale ratio can be constrained from observations, and thus we can test our association of $\langle W_{\rm Mg\,II}\rangle \sim 1$ Å absorbers with turbulence-dominated CGM by checking if these systems indeed have $t_{\rm cool}^{\rm (s)} < t_{\rm ff}$.

Using equations (6)–(8), we get

$$\frac{t_{\rm cool}^{\rm (s)}}{t_{\rm ff}} = \frac{(9/10) m_{\rm p} v_{\rm c}^3}{\sqrt{2} X r \langle n_{\rm H}\rangle \Lambda}\,. \tag{17}$$

Further using $T^{\rm (s)}/10^6\,{\rm K} = 0.45\,v_{100}^2$ where $v_{100} = v_{\rm c}/100\,{\rm km\,s^{-1}}$ (equation 7) and the Gnat & Sternberg (2007) approximation for the cooling function.[3] for gas with metallicity close to solar:

$$\Lambda(T, Z) = 1.7 \cdot 10^{-22} (T/10^6\,{\rm K})^{-0.54} (Z/{\rm Z}_\odot)\,{\rm erg\,cm^3\,s^{-1}}\,, \tag{18}$$

[3]The typical definition of Λ assumes energy losses per unit volume are $\mathcal{L} = n_{\rm e} n_{\rm H} \Lambda$, where $n_{\rm e}$ is the electron density. We converted to our definition ($\mathcal{L} = n_{\rm H}^2 \Lambda$) using $n_{\rm e} = 1.3\,n_{\rm H}$ appropriate for ionized solar metallicity gas.

we get

$$\frac{t_{\rm cool}^{\rm (s)}}{t_{\rm ff}} \approx 0.8\, v_{100}^{4.1} \left(\frac{N_{\rm H}}{10^{19}\,{\rm cm}^{-2}} \cdot \frac{Z}{{\rm Z}_\odot}\right)^{-1}, \quad (19)$$

where we used $T = T^{\rm (s)}$ in equation (18) and replaced $\langle n_{\rm H}\rangle r$ with $\approx (2/\pi) N_{\rm H}$, a relation which is exact for $\langle n_{\rm H}\rangle \propto r^{-2}$. Thus, equation (19) demonstrates that one can estimate $t_{\rm cool}^{\rm (s)}/t_{\rm ff}$ based on a measurement of $v_{\rm c}$ and the metal column density $N_{\rm H}Z$.

To estimate $N_{\rm H}Z$ we use the mean $\rm Si^+$ column $N_{\rm Si^+} = 6 \pm 1 \cdot 10^{14}\,{\rm cm}^{-2}$ measured by Lan & Fukugita (2017), based on mean Si II λ1808 absorption associated with $\langle W_{\rm Mg\,II}\rangle > 1$ Å absorbers at $z \approx 1$. The Si II λ1808 transition is typically optically thin due to its low oscillator strength ($\tau = 0.37$ at line centre for the sightline shown in Figs 1 and 5) and thus the deduced ion column is more robust than when using saturated absorption lines. Given the solar Si/H ratio of $10^{-4.5}$, we thus infer $N_{\rm H}({\rm Z/Z_\odot}) = 2 \pm 0.3 \cdot 10^{19} N_{\rm Si}/N_{\rm Si^+}$. Additionally, the same sample has $v_{\rm c} \approx 140 \pm 20\,{\rm km\,s^{-1}}$, derived from the 1D velocity dispersion of the dark matter halo $\sigma_{\rm dm}$ inferred by Lan & Mo (2018) based on abundance matching, and using $v_{\rm c} = \sqrt{2}\sigma_{\rm dm}$ appropriate for an isothermal potential. We thus get

$$\frac{t_{\rm cool}^{\rm (s)}}{t_{\rm ff}} = 1.7 \frac{N_{\rm Si^+}}{N_{\rm Si}} \left(\frac{v_{\rm c}}{140\,{\rm km\,s^{-1}}}\right)^{4.1} \left(\frac{N_{\rm Si^+}}{6 \cdot 10^{14}\,{\rm cm}^{-2}}\right)^{-1}, \quad (20)$$

where the uncertainties on the derived $v_{\rm c}$ and metal column mentioned above imply a factor of ≈ 2 uncertainty on the derived $t_{\rm cool}^{\rm (s)}/t_{\rm ff}$. For a typical $N_{\rm Si^+}/N_{\rm Si}$ fraction of 0.2 in turbulence-dominated inner CGM in m12i at $z = 1$, the observationally inferred $t_{\rm cool}^{\rm (s)}/t_{\rm ff}$ is thus ≈ 0.2–0.7. This value is smaller than unity, which provides further supporting evidence for our conclusion that $\langle W_{\rm Mg\,II}\rangle \sim 1$ Å absorbers trace turbulence-dominated inner CGM. The result that the inferred ratio is close to unity suggests that these are the most massive galaxies with a turbulence dominated inner CGM at this redshift.

Lan & Mo (2018) also fit a line of sight gas dispersion of $\sigma_{\rm gas} = 105 \pm 10\,{\rm km\,s^{-1}}$ to the mean Mg II absorption profile of their sample. The ratio $\sigma_{\rm gas}/\sigma_{\rm dm} \approx 1$ they deduce can be compared to the $\sigma_{\rm turb}/v_{\rm c} \approx 0.7$–$0.9$ we find in m11 and m12 FIRE galaxies at $z \approx 1$ (Figs 3 and 8). Since $\sigma_{\rm turb} \approx \sqrt{3}\sigma_{\rm gas}$ and $v_{\rm c} \approx \sqrt{2}\sigma_{\rm dm}$, we get $\sigma_{\rm gas}/\sigma_{\rm dm} \approx 0.6$–$0.7$ in FIRE, somewhat lower than deduced by Lan & Mo (2018) from the observations. This difference may be a result of stacking saturated absorption features around galaxies which span a range in mass, which could bias the measured $\sigma_{\rm gas}$ somewhat high relative to the median value in the sample. Alternatively, the turbulent velocity in FIRE could be somewhat underpredicted relative to real galaxies. We leave a more accurate comparison of observed Mg II equivalent widths with those in FIRE to future work.

5 DISCUSSION

5.1 How does hot CGM formation affect galaxy evolution?

It has long been predicted that the formation of a quasi-static hot phase in the CGM is required for galaxy quenching (Kereš et al. 2005; Bower et al. 2006; Croton et al. 2006; Dekel & Birnboim 2006; Somerville et al. 2008). Our results provide direct evidence that these processes are at least correlated, by showing that sightlines through inner CGM prior to hot phase formation are expected to exhibit $\langle W_{\rm Mg\,II}\rangle \sim \langle W_{\rm C\,IV}\rangle \sim 1$ Å, in contrast with after hot phase formation where lower average equivalent widths of $\ll 1$ Å are expected (Figs 7 and 9). Thus the observed $\langle W_{\rm Mg\,II}\rangle \sim 1$ Å around SF galaxies in contrast with $\langle W_{\rm Mg\,II}\rangle \ll 1$ Å around red galaxies (Bowen & Chelouche 2010; Bordoloi et al. 2011; Lan et al. 2014; Huang et al. 2015; Lan & Mo 2018; Anand et al. 2021, see Figs 10 and 11) and evidence for a similar dichotomy in $\langle W_{\rm C\,IV}\rangle$ (Bordoloi et al. 2014; Garza et al. 2025) indicates that in typical $\sim L^*$ blue galaxies a quasi-static hot phase has not yet formed in the inner CGM, while in red galaxies it has.

More recent studies based on the FIRE simulations have argued that hot phase formation in the inner CGM also facilitates the formation of thin galactic discs, while prior to hot phase formation thick disc and irregular morphologies are expected (Yu et al. 2021; Stern et al. 2021a; Hafen et al. 2022; Gurvich et al. 2023; Yu et al. 2023). Observations suggest that thin discs have formed mainly at late times ($z < 1$) and in relatively massive SF galaxies (Kassin et al. 2012; Tiley et al. 2021). If this connection between 'disc settling' and ICV is true, then we expect that massive thin disc galaxies should exhibit $\langle W_{\rm Mg\,II}\rangle \ll 1$ Å and $\langle W_{\rm C\,IV}\rangle \ll 1$ Å in their inner CGM, in contrast with the $W_\lambda \sim 1$ Å seen in the $M_\star \sim 10^{10}\,{\rm M}_\odot$ galaxies which dominate the samples shown in Fig. 10. Such low equivalent widths are indeed inferred in the Milky-Way CGM by (Bish et al. 2021), in M31 by Lehner et al. (2025), and in the most massive blue galaxies at $0.4 < z < 0.7$ by Lan (2020) as discussed above. There is thus tentative evidence to support this suggested scenario, though further comparison of SF galaxy morphologies and $\langle W_{\rm Mg\,II}\rangle$ at small impact parameters are required. The large sample of quasar-absorber pairs upcoming in DESI (Wu et al. 2025) could be useful for this test.

5.2 Implications for CLOUDY modelling of UV absorbers

Observational inference studies based on circumgalactic UV absorbers usually use CLOUDY (Ferland et al. 2017; Chatzikos et al. 2023) to derive properties of absorbing gas structures, including volume and column densities, cloud physical sizes, and gas metallicity (e.g. Prochaska 1999). These studies almost always assume that along a given line of sight and a given velocity relative to the galaxy, the absorbing gas originates in one or more independent clouds, where each cloud has uniform properties, i.e. a single density and metallicity. While this approach is reasonably motivated when UV absorbers are cool clouds embedded in a hot medium (e.g. left panels of Fig. 1) it is inadequate if the hot phase is subdominant and a cool turbulent medium fills the volume. As shown in the right panel of Fig. 2, when the cool gas dominates it has a continuous lognormal density distribution, and thus a different modeling approach is required.

An alternative would be to account for the inherently lognormal density distribution of UV-absorbing gas within the CLOUDY model[4] By comparing observations to a grid of such models with varying mean density $\langle n_{\rm H}\rangle$, density width $\sigma_{\log\rho}$, and total gas mass, one can find the parameters which best describe a given observation set. These best-fitting parameters can then be compared to those in the simulations, thus providing an observational test of the cool and turbulent CGM scenario.

A similar modelling approach was recently suggested by Dutta et al. (2024), though they advocated applying this technique regardless of whether the absorbers originate in thermal pressure-dominated or turbulence-dominated CGM. We emphasize that the density distributions of cool gas in these two regimes are inherently different (see Fig. 2), since in turbulence-dominated CGM the density distribution is a result of the supersonic turbulence, while in thermal-pressure dominated CGM the cool gas density distribution is set by

[4]CLOUDY can model arbitrary density profiles in the absorbers, such as lognormals or power-laws as done in Stern et al. (2016).

the interaction between cool-clouds and the hot background (e.g. the turbulent radiative mixing layers described in Fielding et al. 2020). The free parameter space required to explore absorption from turbulence-dominated CGM as suggested here is thus smaller than the general case proposed by Dutta et al. (2024).

5.3 Implications for small-scale physics of the CGM

Recent theoretical studies of small-scale physics in the CGM have focused on the thermal pressure-dominated scenario, in which cool clouds are embedded in a hot volume-filling background (e.g. Gronke & Oh 2018; McCourt et al. 2018; Fielding et al. 2020; Afruni, Fraternali & Pezzulli 2021; and many others, see review in Faucher-Giguère & Oh 2023). The physics of small-scale structure when a quasi-static hot phase is subdominant as discussed in this work are likely qualitatively different than when it is dominant. For example, when turbulence dominates, the interaction between different temperature phases is driven primarily by ram pressure – rather than by thermal pressure as commonly assumed (e.g. McCourt et al. 2018; Abruzzo, Bryan & Fielding 2022; Gronke et al. 2022). Consequently, observable properties such as cloud coherence scales (e.g. Afruni et al. 2023) and velocity structure functions (e.g. Chen et al. 2023) are expected to differ. Given our results above that turbulence-dominated CGM may be prevalent at inner halo radii of SF galaxies (Fig. 10), further theoretical exploration of small-scale physics in turbulence-dominated CGM would be beneficial.

5.4 Caveats: resolution, cosmic rays, and AGN feedback

It has been argued that the cool gas mass fraction $f_{\rm cool}$ in thermal-pressure dominated CGM depends on simulation resolution (de Voort et al. 2019; Hummels et al. 2019; Peeples et al. 2019; Ramesh & Nelson 2024). We thus cannot strictly rule out a thermal-pressure dominated inner CGM origin for $W_\lambda \sim 1$ Å absorbers. However, in the turbulence-dominated regime we find $f_{\rm cool} \approx 1$ independent of simulation resolution (Fig. B1 and Section 3.6), and thus the predicted absorption equivalent widths induced by cool gas are robust in this regime and consistent with analytic estimates (Section 3.4.1). The turbulence-dominated inner CGM scenario is thus possible to rule out with cool gas observations. The success of this scenario to reproduce observations thus supports its applicability.

We note also that the version of the FIRE simulations used in this study assume ideal hydrodynamics, and in particular do not include cosmic ray (CR) physics. Other FIRE zoom simulations that include CRs with constant diffusion coefficients have shown that CRs can potentially prevent the formation of a volume-filling hot phase at the Milky-Way mass scale at $z < 1$, replacing thermal pressure support with CR pressure support (e.g. Hopkins et al. 2020; Ji et al. 2020; Hopkins et al. 2021; Ji et al. 2021). However, in lower mass galaxies and at $z \gtrsim 1$, CR pressure remains subdominant in such FIRE simulations with CRs. At these masses and redshifts, we find above that inner CGM are dominated by turbulence. The previous analyses of FIRE simulations including CRs suggest that this regime is not qualitatively affected by CR feedback.

A dominance of CR pressure over thermal pressure at the Milky-Way mass scale implies a high-mass fraction of the cool CGM phase, and thus has been suggested as an explanation for the substantial cool gas reservoirs seen in CGM observations of low-redshift $\lesssim L^*$ galaxies (Salem, Bryan & Corlies 2016; Butsky & Quinn 2018; Buck et al. 2020; Butsky et al. 2020; Ji et al. 2020; Butsky et al. 2022; DeFelippis et al. 2024). Our results suggest an alternative explanation, where the high observed cool gas columns are a result of short cooling times in the hot phase, rather than by CR pressure.

The simulations analysed in this work also do not include feedback from AGNs, and thus our results on cool, pre-ICV CGM are strictly applicable only if AGN feedback does not qualitatively change the CGM in this regime. We note that it has long been argued that cool CGM are not strongly affected by AGN feedback, either because the CGM is less susceptible to energy deposition or due to limited BH growth during this early phase (see Introduction above and discussion in Byrne et al. 2023). The ability of pre-ICV CGM to correctly reproduce observed Mg II equivalent width observations around blue galaxies at $0 \lesssim z \lesssim 1.5$ (Fig. 10) may suggest that the effect of AGN feedback on the CGM pre-ICV is indeed small.

6 SUMMARY

This paper continues the investigation of a qualitative transition in the inner CGM ($\sim 0.2 R_{\rm vir}$) of galaxies simulated in FIRE, at which a quasi-static and volume-filling hot phase forms at inner halo radii. This transition has been dubbed 'inner CGM virialization' or ICV, and occurs when the cooling time of hot gas in the inner CGM exceeds the free-fall time, corresponding to the halo mass exceeding a threshold of $\approx 10^{12}$ M$_\odot$. Prior to this transition hot gas which formed via accretion or feedback shocks rapidly cools in the inner CGM, so the inner CGM is dominated by cool inflows and outflows (de Voort et al. 2016; Yu et al. 2021; Stern et al. 2021a, b; Hafen et al. 2022; Byrne et al. 2023; Gurvich et al. 2023; Yu et al. 2023). The current study focuses on implications of this transition for circumgalactic UV absorption at $0 \leq z \lesssim 2$, and specifically we characterize the distinct CGM absorption signatures in pre-ICV galaxies. Our main results can be summarized as follows:

(i) ICV in FIRE corresponds to a transition from supersonic CGM turbulence ($\sigma_{\rm turb} \gg \langle c_{\rm s} \rangle_\rho$) to subsonic CGM turbulence ($\sigma_{\rm turb} \lesssim \langle c_{\rm s} \rangle_\rho$), where $\sigma_{\rm turb}$ and $\langle c_{\rm s} \rangle_\rho$ are respectively the 3D turbulent velocity and mass-weighted sound speed in a given radial shell (Figs 3 and 8). Equivalently, ICV is a transition between turbulence pressure-dominated and thermal pressure-dominated inner CGM (Fig. 4). This conclusion is consistent with previous idealized studies on hot phase formation which accounted for stellar feedback (Fielding et al. 2017; Pandya et al. 2023).

(ii) The transition to subsonic turbulence is driven by an increase in $\langle c_{\rm s} \rangle_\rho$ from 20–30 km s^{-1} to $\gtrsim 100$ km s^{-1} when the hot phase becomes dominant, in contrast with $\sigma_{\rm turb}$ which is roughly constant or even decreases. During the supersonic phase we find $\sigma_{\rm turb}(0.2\ R_{\rm vir}) \sim v_{\rm c}$, where $v_{\rm c}$ is the circular velocity (Figs 3 and 8).

(iii) When turbulence is subsonic, the gas density distribution at a given radius consists of a narrow peak of hot gas with a high density tail due to cool clouds, as in the common CGM paradigm. In contrast, when turbulence is supersonic, the density distribution forms a single wide, roughly lognormal with FWHM approaching 2 dex (Fig. 2). The widths of the density distributions are consistent with expectations from idealized simulations of isothermal turbulence with compressive driving (bottom panel of Fig. 3).

(iv) The nature of UV-absorbing gas changes upon ICV. After ICV, absorbers trace localized cool clouds embedded in a hot CGM as is commonly assumed (e.g. Tumlinson et al. 2017). Prior to ICV, absorption features trace the turbulent and cool volume-filling phase of the inner CGM (Figs 1, 5).

(v) For pre-ICV $\lesssim L^\star$ galaxies at $0 \leq z \lesssim 2$ with turbulence-dominated inner CGM, we predict mean equivalent widths of $\langle W_\lambda \rangle \sim 1$Å at impact parameters $\approx 0.2 R_{\rm vir}$, across a broad range

of strong UV transitions (Mg II, C II-IV, Si II-IV, O III-V), (Figs 6 and 9). These high $\langle W_\lambda \rangle$ are due to the dominance of the cool phase, the large turbulent velocity, and the wide density distribution which entails a wide range of ionization.

(vi) Simulation resolution, at the range probed of 880–57 000 $M_\odot$, does not significantly affect the predicted $\langle W_\lambda \rangle$ prior to ICV. This follows since most of the inner CGM is cool even at low resolution, so increasing resolution does not significantly further increase the mass of the cool phase (Fig. B1).

(vii) Available UV absorption surveys, including COS-Haloes (Werk et al. 2013), zCOSMOS (Bordoloi et al. 2011), SDSS (Lan & Mo 2018; Anand et al. 2021), and DESI (Wu et al. 2025) indicate that SF $\lesssim L^*$ galaxies have order-unity covering fraction of $W_{\rm Mg\,II} \sim 1$ Å absorbers at $R_\perp \approx 0.2 R_{\rm vir}$, consistent with the prediction of turbulence-dominated inner CGM (Fig. 10). Red galaxies exhibit significantly lower mean $W_{\rm Mg\,II}$, inconsistent with turbulence-dominated CGM predictions. This provides direct evidence for a connection between the formation of a quasi-static hot CGM phase and quenching of star formation, as postulated by many previous studies (Kereš et al. 2005; Croton et al. 2006; Dekel & Birnboim 2006; Somerville et al. 2008; Bower et al. 2017; Byrne et al. 2023).

(viii) The Milky-Way exhibits $\langle W_{1548} \rangle \ll 1$ Å (Bish et al. 2021), inconsistent with a turbulence dominated inner CGM, and tentative evidence suggests that low $\langle W_\lambda \rangle$ are common also in M31 (Lehner et al. 2020; Lehner et al. 2025) and in the most massive SF galaxies at $z \approx 0.5$ (Lan 2020). UV absorption signatures thus suggest that massive, low z discs have thermal-energy dominated inner CGM as suggested also by X-ray emission and absorption observations. The inner CGM of these massive low z discs is thus qualitatively distinct from those of blue $\sim L^\star$ galaxies in the survey shown in Fig. 10.

Our results provide a means to identify which galaxies are not surrounded by a quasi-static hot phase, but rather by a predominantly cool, turbulence-dominated inner CGM: such galaxies should exhibit ~ 1 Å equivalent width UV absorption in their inner CGM across a wide range of ions. Based on these results and available observations, we conclude that a quasi-static hot phase in the inner CGM exists only around the most massive SF galaxies (including the Milky-Way and M31) and around quenched galaxies. This result constrains the relation between CGM thermodynamics and the evolution of the central galaxy.

We conclude by noting that most contemporary observational inference studies of the CGM, and studies of small-scale CGM physics, assume the existence of a quasi-static volume-filling hot phase (Sections 5.2 and 5.3). This prevalent assumption is despite that CGM which lack such a hot phase have been predicted in low-mass haloes for decades now, in multiple theoretical studies based on analytic methods, idealized simulations, and cosmological simulations. Given our results above that cool phase-dominated inner CGM are common around SF galaxies, we encourage further study of the theoretical predictions and observational implications of this important, cool and turbulent CGM regime.

ACKNOWLEDGEMENTS

We thank A. Fox, S. D. Johnson, and J. X. Prochaska for insightful conversations which motivated this work, and A. Sternberg for providing comments on a draft version of the manuscript. AK, JS, and RG were supported by the Israel Science Foundation (grant no. 2584/21). CAFG was supported by NSF through grants AST-2108230 and AST-2307327; by NASA through grants 21-ATP21-0036 and 23-ATP23-0008; and by STScI through grant JWST-AR-03252.001-A. Part of this work was performed at the Aspen Center for Physics, which is supported by National Science Foundation grant PHY-2210452. Numerical calculations were run on the Northwestern computer cluster Quest, the Caltech computer cluster Wheeler, Frontera allocation FTA-Hopkins/AST20016 supported by the NSF and TACC, XSEDE/ACCESS allocations ACI-1548562, TGAST140023, and TG-AST140064 also supported by the NSF and TACC, and NASA HEC allocations SMD-16-7561, SMD-17-1204, and SMD-16-7592. In the analysis, we utilized the YT V4.4 toolkit (Turk et al. 2011; The yt Project 2025), the TRIDENT V1.3 code (Hummels et al. 2017; Trident 2025), and the AMIGA HALO FINDER (AHF; Knollmann & Knebe 2009). All analysis scripts were developed in PYTHON 3.10.

DATA AVAILABILITY

A public version of the GIZMO code is available at http://www.tapir.caltech.edu/~phopkins/Site/GIZMO.html. FIRE data products, including FIRE-2 simulation snapshots, initial conditions, and derived data products are available at http://fire.northwestern.edu/data/.

REFERENCES

Abruzzo M. W., Bryan G. L., Fielding D. B., 2022, ApJ, 925, 199
Afruni A., Fraternali F., Pezzulli G., 2021, MNRAS, 501, 5575
Afruni A. et al., 2023, A&A, 680, A112
Aghanim P. C. N., Akrami Y., Ashdown M. et al., 2018, A&A, A6, 641https://doi.org/10.1051/0004-6361/201833910e
Anand A., Nelson D., Kauffmann G., 2021, MNRAS, 504, 65
Anderson M. E., Churazov E., Bregman J. N., 2016, MNRAS, 455, 227
Anglés-Alcázar D., Faucher-Giguère C.-A., Quataert E., 2017, MNRAS, 472, L109 https://doi.org/10.1093/mnrasl/slx161
Behroozi P., Wechsler R. H., Hearin A. P., Conroy C., 2019, MNRAS, 488, 3143
Bhattarai B., Loebman S., Ness M., Cunningham E., Wetzel A., Benincasa S., 2022, BAAS, 54, 6, Bulletin of the AAS --- Issue 6, Abstract 201.07
Birnboim Y., Dekel A., 2003, MNRAS, 345, 349
Bish H. V., Werk J. K., Peek J., Zheng Y., Putman M., 2021, ApJ, 912, 8
Bordoloi R. et al., 2011, ApJ, 743, 10 https://doi.org/10.1088/0004-637X/743/1/10
Bordoloi R. et al., 2014, ApJ, 796, 136
Bowen D. V., Chelouche D., 2010, ApJ, 727, 47
Bower R. G., Benson A. J., Malbon R., Helly J. C., Frenk C. S., Baugh C. M., Cole S., Lacey C. G., 2006, MNRAS, 370, 645
Bower R. G., Schaye J., Frenk C. S., Theuns T., Schaller M., Crain R. A., McAlpine S., 2017, MNRAS, 465, 32
Bregman J. N., Anderson M. E., Miller M. J., Hodges-Kluck E., Dai X., Li J.-T., Li Y., Qu Z., 2018, ApJ, 862, 3
Bregman J. N., Hodges-Kluck E., Qu Z., Pratt C., Li J.-T., Yun Y., 2022, ApJ, 928, 14
Bryan G. L., Norman M. L., 1998, ApJ, 495, 80
Buck T., Pfrommer C., Pakmor R., Grand R. J. J., Springel V., 2020, MNRAS, 497, 1712
Butsky I. S., Quinn T. R., 2018, ApJ, 868, 108
Butsky I. S., Fielding D. B., Hayward C. C., Hummels C. B., Quinn T. R., Werk J. K., 2020, ApJ, 903, 77
Butsky I. S. et al., 2022, ApJ, 935, 69
Byrne L., Faucher-Giguère C.-A., Stern J., Anglés-Alcázar D., Wellons S., Gurvich A. B., Hopkins P. F., 2023, MNRAS, 520, 1, 722,
Chatzikos M. et al., 2023, RMxAA, 59, 327
Chen H.-W., Helsby J. E., Gauthier J.-R., Shectman S. A., Thompson I. B., Tinker J. L., 2010, ApJ, 714, 1521

Chen H.-W. et al., 2023, ApJ, 955, L25
Cherrey M. et al., 2025, A&A, 694, A117
Croton D. J. et al., 2006, MNRAS, 365, 11
DeFelippis D., Bournaud F., Bouché N., Tollet E., Farcy M., Rey M., Rosdahl J., Blaizot J., 2024, MNRAS, 530, 52
Dekel A., Birnboim Y., 2006, MNRAS, 368, 2
Draine B. T., 2011, Physics of the Interstellar and Intergalactic Medium. Princeton University Press, Princeton, NJ, https://press.princeton.edu/books/paperback/9780691122144/physics-of-the-interstellar-and-intergalactic-medium
Dutta A., Bisht M. S., Sharma P., Ghosh R., Roy M., Nath B. B., 2024, MNRAS, 531, 5117
Dutton A. A., Macciò A. V., 2014, MNRAS, 441, 3359
El-Badry K., Quataert E., Wetzel A., 2018, MNRAS, 473, 1930https://doi.org/10.1093/mnras/stx2482
Escala I. et al., 2018, MNRAS, 474, 2194
Faerman Y., Sternberg A., McKee C. F., 2020, ApJ, 893, 82
Faucher-Giguère C.-A., Oh S. P., 2023, ARA&A, 61, 131
Faucher-Giguère C.-A., Lidz A., Zaldarriaga M., Hernquist L., 2009, PASP, 703, 1416https://doi.org/10.1088/0004-637X/703/2/1416
Ferland G. J., Korista K. T., Verner D. A., 1998, PASP, 110, 761https://doi.org/10.1086/316190
Ferland G. J. et al., 2017, RMxAA, 53, 385
Fielding D., Quataert E., McCourt M., Thompson T. A., 2017, MNRAS, 466, 3810
Fielding D. B., Ostriker E. C., Bryan G. L., Jermyn A. S., 2020, ApJ, 894, L24
Garrison-Kimmel S. et al., 2017, MNRAS, 471, 1709
Garrison-Kimmel S. et al., 2019, MNRAS, 487, 1380
Garza S. L., Werk J. K., Berg T. A. M., Faerman Y., Oppenheimer B. D., Bordoloi R., Ellison S. L., 2025, ApJL, 978, L12,
Gnat O., Sternberg A., 2007, ApJS, 168, 213
Gronke M., Oh S. P., 2018, MNRAS, 480, L111
Gronke M., Oh S. P., Ji S., Norman C., 2022, MNRAS, 511, 859
Gurvich A. B. et al., 2023, MNRAS, 519, 2https://doi.org/10.1093/mnras/stac3712
Haardt F., Madau P., 2012, ApJ, 746, 125
Hafen Z. et al., 2022, MNRAS, 514, 5056
Holguin F., Hayward C. C., Ma X., Anglés-Alcázar D., Cochrane R. K., 2024, preprint (arXiv:2405.13110)
Hopkins P. F., 2015, MNRAS, 450, 53
Hopkins P. F., 2017, MNRAS, 466, 3387
Hopkins P. F., Narayanan D., Murray N., 2013, MNRAS, 432, 2647
Hopkins P. F., Kereš D., Oñorbe J., Faucher-Giguère C.-A., Quataert E., Murray N., Bullock J. S., 2014, MNRAS, 445, 581
Hopkins P. F. et al., 2018, MNRAS, 480, 800
Hopkins P. F. et al., 2020, MNRAS, 492, 3465
Hopkins P. F., Squire J., Chan T. K., Quataert E., Ji S., Kereš D., Faucher-Giguère C.-A., 2021, MNRAS, 501, 4184
Hopkins P. F. et al., 2023, MNRAS, 519, 3154
Huang Y.-H., Chen H.-W., Johnson S. D., Weiner B. J., 2015, MNRAS, 455, 1713
Huang Y.-H., Chen H.-W., Shectman S. A., Johnson S. D., Zahedy F. S., Helsby J. E., Gauthier J.-R., Thompson I. B., 2021, Monthly Notices of the Royal Astronomical Society, 502, 4743https://doi.org/10.1093/mnras/stab360
Hummels C. B., Smith B. D., Silvia D. W., 2017, ApJ, 847, 59
Hummels C. B. et al., 2019, ApJ, 882, 156
Ji S. et al., 2020, MNRAS, 496, 4221
Ji S., Kereš D., Chan T. K., Stern J., Hummels C. B., Hopkins P. F., Quataert E., Faucher-Giguère C.-A., 2021, MNRAS, 505, 259
Johnson S. D., Chen H.-W., Mulchaey J. S., Schaye J., Straka L. A., 2017, ApJ, 850, L10
Kassin S. A. et al., 2012, ApJ, 758, 106
Kereš D., Katz N., Weinberg D. H., Davé R., 2005, MNRAS, 363, 2
Knollmann S. R., Knebe A., 2009, ApJS, 182, 608https://doi.org/10.1088/0067-0049/182/2/608
Kroupa P., 2001, MNRAS, 322, 231 https://doi.org/10.1046/j.1365-8711.2001.04022.x
Krumholz M. R., 2014, Phys. Rep., 539, 49
Lan T.-W., 2020, ApJ, 897, 97
Lan T.-W., Fukugita M., 2017, ApJ, 850, 156
Lan T.-W., Mo H., 2018, ApJ, 866, 36 https://doi.org/10.3847/1538-4357/aadc08
Lan T.-W., Ménard B., Zhu G., 2014, ApJ, 795, 31
Lehner N. et al., 2020, ApJ, 900, 9 https://doi.org/10.3847/1538-4357/aba49c
Lehner N. et al., 2025, preprint (arXiv:2506.16573)
Leitherer C., Schaerer D., Goldader J. D., 1999, ApJS, 123, 3 , https://doi.org/10.1086/313233
Li F. et al., 2021, MNRAS, 500, 1038
Liang C. J., Chen H.-W., 2014, MNRAS, 445, 2061
Lochhaas C., Bryan G. L., Li Y., Li M., Fielding D., 2020, MNRAS, 493, 1461
Lopez S. et al., 2020, MNRAS, 491, 4442 https://doi.org/10.1093/mnras/stz3183
Manuwal A., Narayanan A., Udhwani P., Srianand R., Savage B. D., Charlton J. C., Misawa T., 2021, MNRAS, 505, 3635
McCourt M., Oh S. P., O'Leary R., Madigan A.-M., 2018, MNRAS, 473, 5407
Mo H., Chen Y., Wang H., 2024, MNRAS, 532, 3808
Mortensen K., C. K. V. G., Jones T., Faucher-Giguère C.-A., Sanders R. L., Ellis R. S., Leethochawalit N., Stark D. P., 2021, ApJ, 914, 92 https://doi.org/10.3847/1538-4357/abfa11
Nielsen N. M., Churchill C. W., Kacprzak G. G., 2013, ApJ, 776, 115
Oren Y., Sternberg A., McKee C. F., Faerman Y., Genel S., 2024, ApJ, 974, 291,
Pandya V. et al., 2023, ApJ, 956, 118
Peeples M. S. et al., 2019, ApJ, 873, 129
Pezzulli G., Fraternali F., Binney J., 2017, MNRAS, 467, 311
Prochaska J. X., 1999, ApJ, 511, L71
Ramesh R., Nelson D., 2024, MNRAS, 528, 3320
Rees M. J., Ostriker J. P., 1977, MNRAS, 179, 541
Salem M., Bryan G. L., Corlies L., 2016, MNRAS, 456, 582
Sales L. V., Navarro J. F., Theuns T., Schaye J., White S. D. M., Frenk C. S., Crain R. A., Dalla Vecchia C., 2012, MNRAS, 423, 1544
Samuel J. et al., 2020, MNRAS, 491, 1471
Schroetter I. et al., 2021, MNRAS, 506, 1355
Silk J., 1977, ApJ, 211, 638
Singh P., Lau E. T., Faerman Y., Stern J., Nagai D., 2024, MNRAS, 532, 3222
Somerville R. S., Hopkins P. F., Cox T. J., Robertson B. E., Hernquist L., 2008, MNRAS, 391, 481
Sormani M. C., Sobacchi E., Pezzulli G., Binney J., Klessen R. S., 2018, MNRAS, 481, 3370
Spitzer Lyman J., 1956, ApJ, 124, 20
Springel V., 2005, MNRAS, 364, 1105 https://doi.org/10.1111/j.1365-2966.2005.09655.x
Stern J., Hennawi J. F., Prochaska J. X., Werk J. K., 2016, ApJ, 830, 87
Stern J., Fielding D., Faucher-Giguère C.-A., Quataert E., 2019, MNRAS, 488, 2549
Stern J., Fielding D., Faucher-Giguère C.-A., Quataert E., 2020, MNRAS, 492, 6042
Stern J. et al., 2021b, MNRAS, 507, 2869 https://doi.org/10.1093/mnras/stab2240
Stern J. et al., 2021a, ApJ, 911, 88
Stern J., Fielding D., Hafen Z., Su K.-Y., Naor N., Faucher-Giguère C.-A., Quataert E., Bullock J., 2024, MNRAS, 530, 1711
Sultan I., Faucher-Giguère C.-A., Stern J., Rotshtein S., Byrne L., Wijers N., 2024, preprint (arXiv:2410.16359)
The yt Project, 2025, yt: Pythonic Data Analysis and Visualization for Astrophysical Simulation Data, https://yt-project.org/doc/index.html (accessed 30 Sep 2025)
Theuns T., 2021, MNRAS, 500, 2741
Tiley A. L. et al., 2021, MNRAS, 506, 323

Trident, 2025, Trident Documentation, https://trident.readthedocs.io/en/latest/ (accessed 30 Sep 2025)
Tumlinson J., Peeples M. S., Werk J. K., 2017, ARA&A, 55, 389
Turk M. J., Smith B. D., Oishi J. S., Skory S., Skillman S., Abel T., Norman M. L., 2011, ApJS, 192, 9
van de Voort F., Quataert E., Hopkins P. F., Faucher-Giguère C.-A., Feldmann R., Kereš D., Chan T. K., Hafen Z., 2016, MNRAS, 463, 4533
van de Voort F., Springel V., Mandelker N., van den Bosch F. C., Pakmor R., 2019, MNRAS, 482, L85
Werk J. K., Prochaska J. X., Thom C., Tumlinson J., Tripp T. M., O'Meara J. M., Peeples M. S., 2013, ApJS, 204, 17https://doi.org/10.1088/0067-0049/204/2/17
Wetzel A. R., Hopkins P. F., Kim J.-h., 2016, ApJ, 827, L23 https://doi.org/10.3847/2041-8205/827/2/L23
White S. D. M., Frenk C. S., 1991, ApJ, 379, 52
White S. D. M., Rees M. J., 1978, MNRAS, 183, 341
Wiersma R. P. C., Schaye J., Smith B. D., 2009, MNRAS, 393, 99
Wu X. et al., 2025, ApJ, 983, 186,
Yu S. et al., 2021, MNRAS, 505, 1, 889
Yu S. et al., 2023, MNRAS, 523, 6220

APPENDIX A: GAS DENSITY DISTRIBUTIONS AT $0.5R_{\rm VIR}$

Fig. A1 plots the mass-weighted gas density distributions at $r = 0.5R_{\rm vir}$ for the two snapshots shown in Fig. 2. As above, we include all gas resolution elements in a thin spherical shell of width $\delta r = 0.01\ R_{\rm vir}$ without any selection on temperature. Colour denotes the mass-weighted average $\log T$ of gas at each density bin, and the top axis notes the overdensity $\rho/\bar{\rho}$. In the post-ICV $z = 0$ snapshot (top panel), the hot low-density gas dominates with a relatively narrow dispersion of $\sigma_{\log\rho} \approx 0.2$ dex, as expected due to the high $t^{(s)}_{\rm cool} = 26\,t_{\rm ff}$ at this radius and redshift. In the pre-ICV snapshot at $z = 0.75$ (bottom panel), the hot gas is still dominant since the outer CGM has already virialized (Stern et al. 2021a). There is though a significantly more prominent cool gas phase than seen at $z = 0$, perhaps due to the lower $t^{(s)}_{\rm cool}/t_{\rm ff} = 5$, or due to the effect of bursty feedback on the outer CGM prior to ICV.

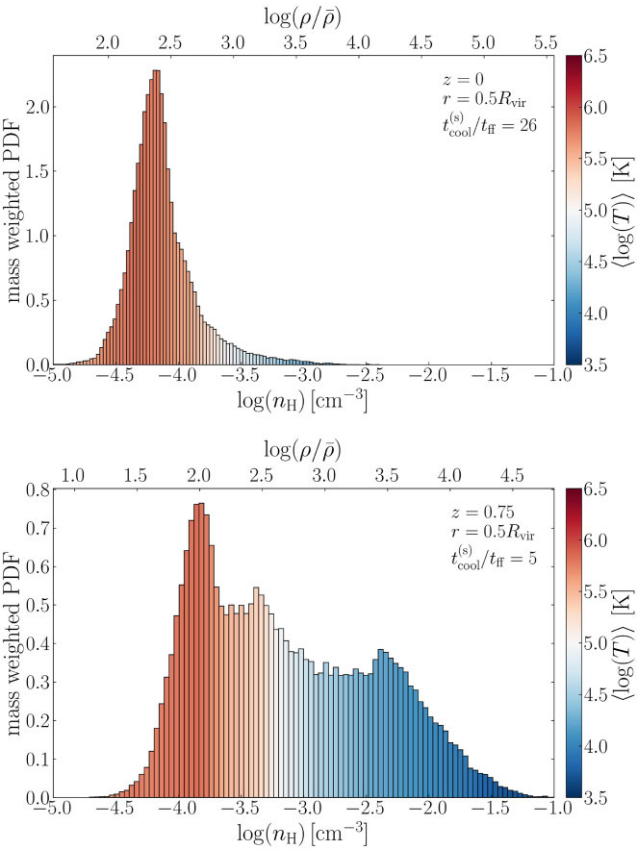

Figure A1. Similar to Fig. 2, for $r = 0.5\ R_{\rm vir}$. Panels show mass-weighted gas density distributions in a thin shell in the m12i simulation at $z = 0$ (top) and at $z = 0.75$ (bottom). Colour indicates average temperature at each density bin. In both snapshots, hot gas dominates the mass consistent with $t^{(s)}_{\rm cool} > t_{\rm ff}$ (noted), though with a significantly more prominent cool gas phase at $z = 0.75$.

APPENDIX B: RESOLUTION DEPENDENCE

Fig. B1 explores how our results depend on simulation resolution as discussed in Section 3.6, utilizing the three FIRE-m12i simulations with baryon mass resolution of $m_b = 880\,M_\odot$ (left panels), $7100\,M_\odot$ (fiducial value, middle panels) and $57\,000\,M_\odot$ (right panels). Top two rows are similar to the two top panels of Fig. 3, while the bottom row shows the mean equivalent width of Mg II and the ratio $t_{cool}^{(s)}/t_{ff}$ derived using equations (6)–(8).

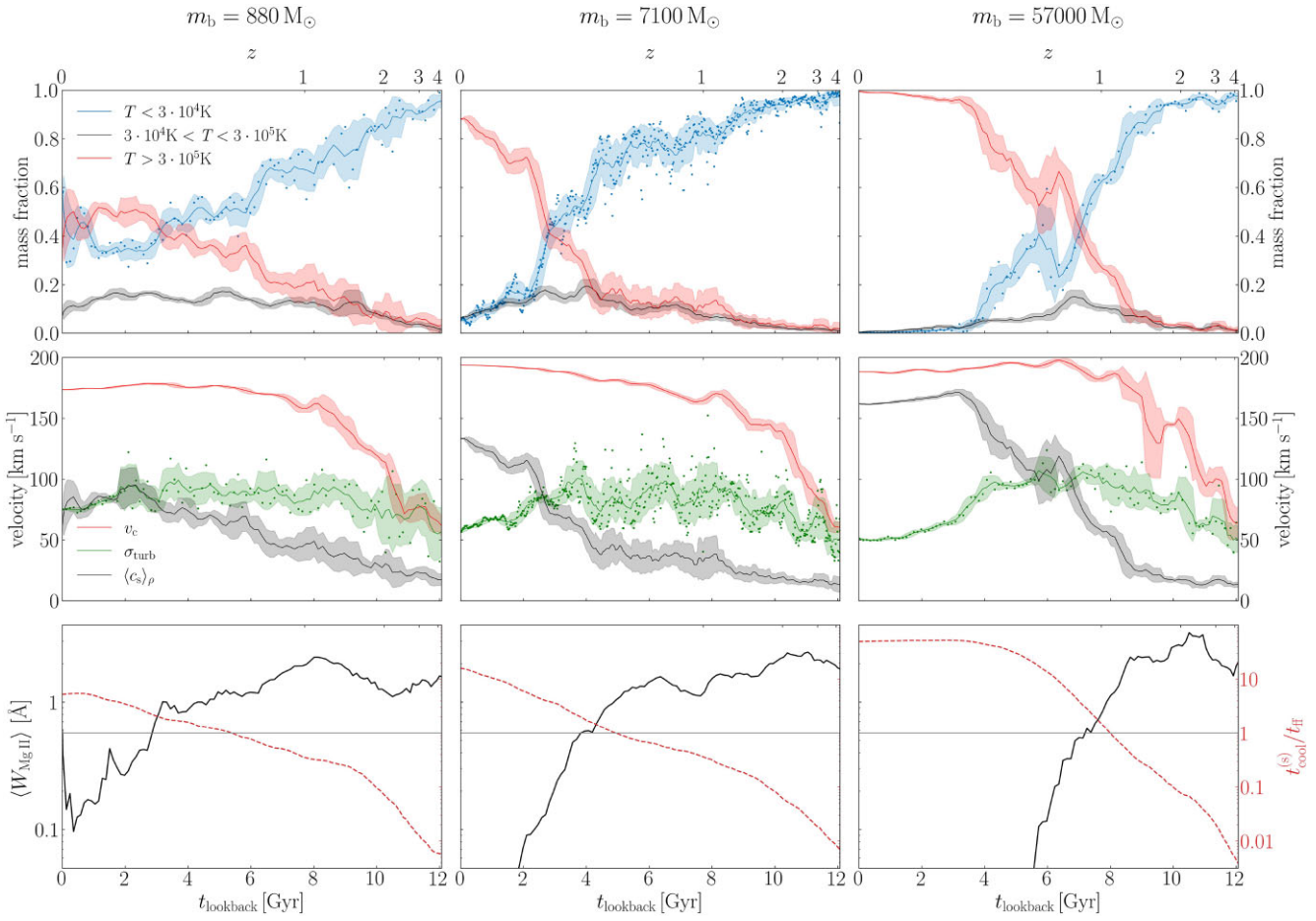

Figure B1. The evolution of gas properties at $r = 0.2\,R_{vir}$ versus simulation resolution (noted on top) in the FIRE-m12i halo. Top row: Gas mass fractions in three temperature bins. Lines and shaded regions indicate running means and dispersions, while dots indicate individual snapshots (shown only for the cool phase). Middle row: Circular velocity (red), turbulent velocity (green), and mass-weighted sound speed (black). Bottom row: Mean equivalent width of Mg II (solid black, left axis) and the ratio $t_{cool}^{(s)}/t_{ff}$ (dashed red, right axis). Grey horizontal line marks $t_{cool}^{(s)} = t_{ff}$. The panels show that v_c and thus $t_{cool}^{(s)}/t_{ff} \propto v_c^4$ increase somewhat more slowly at higher resolution, and hence ICV occurs somewhat later. At all resolutions we find that prior to ICV when $t_{cool}^{(s)} < t_{ff}$, cool gas dominates the mass, turbulence is supersonic, and $\langle W_{Mg\,ii} \rangle \gtrsim 1$ Å. Our main conclusions are thus independent of resolution at the range probed.

APPENDIX C: OBSERVED $\langle W_{\rm MgII}\rangle$

In this appendix, we provide details on observed $\langle W_{\rm MgII}\rangle$ gathered from the literature and plotted in Figs 10 and 11. The relevant values are listed in Table 3. Calculations of $R_{\rm vir}$ are based on Behroozi et al. (2019) to estimate $M_{\rm halo}$ from $M_\star$ and z, and assume an NFW profile with concentration parameter from Dutton & Macciò (2014) to calculate $R_{\rm vir}$ from $M_{\rm halo}$.

(i) zCOSMOS (Bordoloi et al. 2011): $\langle W_{\rm MgII}\rangle$ is measured on co-added background *galaxy* spectra obtained with the LR blue grism on VLT (resolution $R\sim200$). Co-added spectra are derived for different impact parameters from the foreground galaxy, and for different foreground galaxy masses and types. For both mass bins of the SF galaxies and the low-mass bin of the red galaxies the median $0.2\,R_{\rm vir}$ is in the range 26–38 kpc, so we use their $\langle W_{\rm MgII}\rangle$ measurement in the smallest impact parameter bin of $R_\perp=0$–50 kpc. The high-mass red galaxy bin has a median $0.2\,R_{\rm vir}=81$ kpc, so we use the $R_\perp=65-80$ kpc bin.

(ii) COS-haloes (Werk et al. 2013): $W_{Mg\,ii}$ is measured with Keck/HIRES spectra of the background quasars (resolution 6 km s^{-1}, FWHM). This sample includes 26 SF galaxies, of which only three are at $0.15<R_\perp/R_{\rm vir}<0.25$ (see Fig. 12). We use $\langle W_{\rm MgII}\rangle=1.14\pm0.55$ Å based on these three objects. The seven objects with lower $R_\perp/R_{\rm vir}$ have a similar $\langle W_{\rm MgII}\rangle=1.2\pm0.3$ Å, while the five objects with $0.25<R_\perp/R_{\rm vir}<0.35$ have a lower $\langle W_{\rm MgII}\rangle=0.23\pm0.07$ Å.

(iii) SDSS (Lan & Mo 2018): $\langle W_{\rm MgII}\rangle$ are measured on composite SDSS spectra (resolution 150 km s^{-1}) from the DR14 quasar catalogue. Foreground galaxies include emission-line galaxies and LRGs from the BOSS and eBOSS surveys. We use the median $M_\star$ of each survey to calculate $R_\perp=0.2\,R_{\rm vir}$ and then derive $\langle W_{\rm MgII}\rangle(R_\perp=0.2R_{\rm vir})$ by interpolating the $\langle W_{\rm MgII}\rangle$ versus $R_\perp$ relation deduced in Lan & Mo.

(iv) SDSS (Anand et al. 2021): Mg II is detected in individual spectra. We calculate $\langle W_{\rm MgII}\rangle$ by taking the reported average $W_{Mg\,ii}$ for detected objects (>0.4 Å) and multiplying by the reported covering factor.

(v) DESI (Wu et al. 2025): Background quasars and foreground SF galaxies are selected from the DESI internal release 'Iron', with the foreground galaxies divided into two redshift bins. $\langle W_{\rm MgII}\rangle$ are measured both on stacked and individual spectra (resolution ≈100 km s^{-1}). We use the median $M_\star$ and z of each redshift bin to calculate $R_\perp=0.2\,R_{\rm vir}$, and then derive $\langle W_{\rm MgII}\rangle(R_\perp=0.2R_{\rm vir})$ by interpolating the $\langle W_{\rm MgII}\rangle$ versus $R_\perp$ relation deduced in Wu et al.

(vi) Huang et al. (2021): $\langle W_{\rm MgII}\rangle$ measured in MagE spectra of background quasars (resolution ≈70 km s^{-1}, FWHM) on the Magellan Clay Telescope. Foreground galaxies are selected from SDSS DR6 (see Chen et al. 2010 for survey design). We use the value and uncertainty from their derived $W_{\lambda2796}$ versus $R_\perp/R_{\rm vir}$ relation to derive $W_{\lambda2796}(0.2R_{\rm vir})$ and multiply by two to get $\langle W_{\rm MgII}\rangle$, as expected if the lines are fully saturated. Their mean relation for isolated galaxies is consistent with that found by the MAGIICAT survey (Nielsen et al. 2013).

(vii) MEGAFLOW (Cherrey et al. 2025): A sample based on the combination of MUSE galaxy observations and Ultraviolet and Visible Echelle Spectrograph observations of 22 quasar fields. We use the median $M_\star$ of objects at $R_\perp<50$ kpc to calculate $R_\perp=0.2\,R_{\rm vir}$ and then derive $W_{2796}(R_\perp=0.2R_{\rm vir})$ by interpolating their W_{2796} versus $R_\perp$ relation and multiplying by two to get $\langle W_{\rm MgII}\rangle$.

(viii) Gravitational arcs (Lopez et al. 2020; Mortensen et al. 2021): Two galaxies which inner CGM are probed by multiple sightlines towards background gravitationally lensed arcs. We use the $W_{2796}(R_\perp)$ relation deduced from the SW arc in Lopez et al. (2020) and both arcs in Mortensen et al. (2021), while for $0.2R_{\rm vir}$ we use the estimates of 25 kpc and 27 kpc in the papers. We calculate $\langle W_{\rm MgII}\rangle$ using $\langle W_{\rm MgII}\rangle=2W_{2796}(0.2R_{\rm vir})$, as expected if the lines are fully saturated.

This paper has been typeset from a TEX/LATEX file prepared by the author.